An Environmental Cost Basis for Regulating Aviation NO_x Emissions

by

Cassandra Joy Miller

B.S. Aeronautical and Mechanical Engineering
Clarkson University, 2013

SUBMITTED TO THE DEPARTMENT OF AERONAUTICS AND ASTRONAUTICS IN PARTIAL FULFILLMENT OF THE REQUIREMENTS FOR THE DEGREE OF

MASTER OF SCIENCE IN AERONAUTICS AND ASTRONAUTICS

AT THE
MASSACHUSETTS INSTITUTE OF TECHNOLOGY
JUNE 2019

Signature of Author: ____

Department of Aeronautics and Astronautics
May 16, 2019

Certified by: ____

Steven R.H. Barrett
Associate Professor of Aeronautics and Astronautics
Thesis Supervisor

Accepted by: ____

Sertac Karaman
Associate Professor of Aeronautics and Astronautics
Chair, Graduate Program Committee

An Environmental Cost Basis for Regulating Aviation NO_x Emissions

by

Cassandra Joy Miller

Submitted to the Department of Aeronautics and Astronautics
on May 16, 2019 in Partial Fulfilment of the
Requirements for the Degree of Master of Science in
Aeronautics and Astronautics

Abstract

Nitrogen oxides and carbon dioxide are two by-products of combustion in aircraft engines, and have different impacts on the environment. Nitrogen oxides (NO_x) are both an air quality concern and an indirect contributor to radiative forcing, while carbon dioxide (CO_2) is a long-lived greenhouse gas.

The International Civil Aviation Organization has been responsible for evaluating and setting commercial aircraft NO_x emissions standards since 1981. Each of the historical standards has been more stringent than the previous and, when implemented, requires newly certified engines to produce less NO_x per unit rated thrust. Each iteration has been defined as a function of engine overall pressure ratio, which then links the engine cycle, and implicitly fuel burn and CO_2 emissions, to allowable NO_x levels

These regulations have historically been evaluated and implemented with a focus on reducing adverse air quality impacts around airports, but the thermodynamic tradeoff with CO_2 requires additional analysis to quantify net climate impacts. This paper introduces a social cost basis for evaluating aviation NO_x emissions regulations, and quantifies air quality damage, climate damage, and fuel costs associated with allowable emission levels. The result is monetized environmental and fuel costs associated with certain emission standards.

Results show higher overall pressure ratio engines operating at the current NO_x regulatory limit are allowed more environmental damage per unit rated thrust than lower overall pressure ratio engines, therefore allowing uneven social costs per unit thrust (i.e. fuel and environmental costs combined) across the engine design space. This is a consequence of the definition of the regulation today, where higher pressure ratio engines are allowed higher NO_x emissions. Alternative regulation definitions are evaluated which consider the engine cycle and combustor together. Achieving constant social costs requires the regulation to decrease in slope at higher pressure ratios, corresponding to the diminishing marginal efficiency improvements, instead of increasing slope in that region.

Thesis Supervisor: Steven R.H. Barrett
Title: Associate Professor of Aeronautics and Astronautics

Acknowledgements

I'd like to thank my advisor Steven Barrett for giving me the opportunity to join the Laboratory for Aviation and the Environment at MIT, and for supporting me throughout this process. His vision, knowledge, and guidance have allowed me to develop my passion for environmental analysis while staying in my area of technical expertise. I'd like to further thank the greater leadership team in LAE, specifically Ray Speth and Jayant Sabnis whom I worked closely with over the last several years on this project.

I'd also like to thank GE Aviation for providing the funding to complete my degree. The Edison Engineering Development Program gave me the opportunity to further my education, and the flexibility to pick a research topic in my area of interest. Specifically I'd like to thank the ACE leadership team and my direct managers, Phil Weed, Scott Hannula, and Stuart Mueller, who allowed me to continuously change my work schedule so I could attend classes and LAE meetings.

I'd like to thank my LAE lab-mates for being understanding of my work priorities, and for being willing to answer questions via email while I am off campus. I'd like to thank my Edison classmates, who completed two years of course work with me, and are understanding of my school commitments. And I'd like to thank my hockey teammates and friends, for giving me a space where I can take much needed breaks from my professional commitments.

Finally, I'd like to thank my family for always supporting me. My brothers Corey and Dustin have always encouraged me to be competitive, and without them I wouldn't know how to push myself to find my full potential. Last but certainly not least, I'd like to thank my parents David and Pam, who have encouraged me at every step while I've completed this degree. Without their love and support I wouldn't be where I am today.

Contents

List of Figures

List of Tables

Nomenclature

Abbreviations	
AEIC	Aviation Emissions Inventory Code
BFFM2	Boeing Fuel Flow Method 2
CAEE	Committee on Aircraft Engine Emissions
CAEP	Committee on Aviation Environmental Protection
EDB	ICAO Aircraft Engine Emissions Databank
EI	Emissions Index
ICAO	International Civil Aviation Organization
ISA	International Standard Atmosphere
LCV	Lower Calorific Value
LHV	Lower Heating Value
LTO	Landing and Take-Off Operation, <3,000ft
MTOM	Maximum Take-Off Mass
RF	Radiative Forcing
RQL	Rich-Quench-Lean Combustor
SFC	Specific Fuel Consumption
TALON X	Technology for Advanced Low NO_x
TAPS	Twin Annular pre-Mixing Swirler
Chemical Equations & Symbols	
CH_4	Methane
CO_2	Carbon Dioxide
c_p	Specific Heat
D	Flow Path Diameter
D_p	Mass of Emissions Measured in LTO
ER_{cr}	Mass Emissions Rate in Cruise Operation
F_{oo}	Sea-Level Static Rated Thrust
LR	Lapse Rate from Cruise to Rated Thrust
$\dot{m}$	Mass Flow Rate
NO_x	Nitrogen Oxide
O_3	Ozone
OPR, π_{oo}	Engine Overall Pressure Ratio
P_{02}	Stagnation Pressure at Inlet
P_2	Static Pressure at Inlet
$PM_{2.5}$	Particulate Matter
PR	Pressure Ratio

Ps	Static Atmospheric Pressure
T_{02}	Stagnation Temperature at Inlet
T_2	Static Temperature at Inlet
T_4	Static Temperature at Combustor Exit
Ts	Static Atmospheric Temperature
W_f	Fuel Flow Rate
η	Efficiency
γ	Heat Capacity Ratio
Subscripts	
Comp	Compressor
Cr	Cruise
f	fuel
Prop	Propulsive
SL	Sea Level
Trb	Turbine

Introduction

In 1981, the International Civil Aviation Organization (ICAO) adopted the first set of NO_x emission standards for commercial aircraft, restricting NO_x emissions during landing and take-off (LTO) with an aim to reduce adverse air quality impacts near airports. This policy was defined in terms of total NO_x emissions below 3,000 ft per unit rated thrust (D_p/F_{oo}), as a function of engine overall pressure ratio (OPR, π_{oo}). In the years since, four more stringent standards have been adopted, shown in Figure 1, the latest being in 2011 (ICAO, 2008).

NO_x has historically been regarded as a local air quality concern around airports due to its role in the formation of particulate matter ($PM_{2.5}$) and ozone (O_3). More recent research has shown that $PM_{2.5}$ and O_3 attributable to cruise NO_x emissions are also a significant contributor to premature mortalities. Eastham and Barrett (2016) estimated that ~6,800 premature mortalities per year can be attributable to O_3, while $PM_{2.5}$ contributes ~9,200 from current aircraft operations. Barrett et al. (2010) estimated that ~80% of aviation premature mortalities are attributed to cruise and ~20% to LTO. Yim et al. (2015) found aviation-attributed $PM_{2.5}$ and O_3 exposure results in ~16,000 premature mortalities, with 75% attributed to cruise operation. The studies indicate that aviation air quality impacts from cruise are greater than LTO operations.

NO_x emissions also have climate impacts arising from short term ozone production (warming), long-term methane destruction (cooling), long-term ozone depletion (cooling), and formation of nitrate aerosols (cooling) (Grobler et al., 2019). It is estimated the aviation industry currently accounts for 5% of global anthropogenic radiative forcing (RF) (Lee et al., 2009).

NO_x emission levels are a function of engine combustor design (residence time, mixing rates, equivalence ratios, and temperatures), and also a function of the overall engine cycle design which sets the combustor inlet and exit temperatures. Aircraft fuel burn and CO_2 emissions are determined by the engine cycle, with higher OPR and higher temperature cycles providing higher efficiency, and therefore lower fuel consumption and CO_2 emissions. However, as described by the Zeldovich mechanism, higher temperatures increase the rate of thermal NO formation, which is the dominant NO_x production mechanism in gas turbine engines (Kundu et al., 2013). Kyprianidis et al. (2017) showed for rich-burn quick-quench lean-burn (RQL) combustors NO_x increases exponentially with OPR.

Due to this relationship between the engine cycle and NO_x formation, each iteration of the ICAO NO_x standard has set allowable NO_x emission levels as a function of OPR, with the result being that a given combustor will have similar margins to the standard when used in engines with different OPR. This approach creates a tradeoff between engine efficiency and NO_x-related environmental impacts that must be considered in the design of aircraft engines.

Freeman et al. (2018) discuss this NO_x/CO_2 tradeoff in the context of climate impacts, and aim to find a climate "breakeven" point for total RF given different scenarios. It is shown that by decreasing NO_x emissions by 20% (per updated policy) and increasing CO_2 emissions by 2% (per assumed technological tradeoffs required to meet that policy today) as compared to a baseline case, total warming actually increases. This highlights a risk of further restricting NO_x emissions without understanding the resulting engine cycle impacts and resultant CO_2 emissions.

There are limitations to this paper that should be expanded upon. First, the impacts of emission levels are limited to a climate analysis, rather than including air quality and additional fuel costs. There is also an assumed fuel burn increase as a result of limiting NO_x emission levels. Airlines, and therefore engine manufactures, would likely not choose to increase fuel burn rates to offset NO_x emissions, but would instead change the engine cycle or combustor design to meet NO_x standards.

While this thesis also evaluates the CO_2 and NO_x tradeoff for gas turbines, it specifically aims to quantify social costs associated with the current LTO NO_x regulation, and is the first study to incorporate climate damages, air quality damages, and the marginal cost of fuel production into a social cost per unit thrust analysis of the current LTO NO_x regulation. This thesis shows that the regulation as it is defined today allows for uneven environmental damage per unit thrust across a range of OPRs by allowing engines to do more damage as OPR is increased. Additionally, this thesis assesses alternative potential definitions of the regulation which would result in more evenly distributed social costs (i.e. environmental and fuel combined) across the engine design space.

The analysis is organized as follows. The materials and methods section assesses known emission rates, reported for uninstalled, sea level static engines in certification, and outlines techniques used to quantify unknown emission rates, primarily in cruise operation. Then, the social cost of engine operation is quantified, defined as the sum of the marginal cost of fuel production, and climate and air quality damages associated with emissions. Finally, the split between time in LTO and time in cruise are used to determine full-flight impacts.

Several sources of emissions and cost data are used for this analysis. The ICAO Aircraft Engine Emissions Databank (EDB) is used to estimate landing and take-off emissions. The Aviation Emissions Inventory Code (AEIC) and the Boeing Fuel Flow Method 2 (BFFM2) are used to estimate cruise emissions. The historical price of jet fuel and markup rates are used to estimate fuel costs. Damage estimates associated with NO_x and CO_2 emissions are based on an analysis using the Aviation Environmental Portfolio Management Tool. Finally, an uncertainty analysis from all data sources is included in a Monte Carlo simulation, where 95% confidence intervals are presented.

Results display the allowable emissions associated with the CAEP/8 standard, and show the distribution of social costs from those emissions as a function of OPR. Future goals set by the ICAO Committee on Aviation Environmental Protection (CAEP) are also analyzed, and finally an analysis is presented to remove the social cost biases associated with OPR.

Materials & Methods

The main unknown parameters of this analysis are NO_x and CO_2 emissions from current and future aircraft engine technology. There are two modes of operation where emissions must be determined, LTO and cruise, making four unknowns: LTO and cruise NO_x emissions, and LTO and cruise CO_2 emissions. However, engine performance data is proprietary and not widely available.

Throughout this analysis all estimates of emissions for LTO operation are a result of measured data from the ICAO EDB. Since there is no equivalent database for aircraft emissions at altitude, extrapolation techniques and cycle analyses must be used to represent emissions in the space they operate most of the time. Uncertainty in each set of parameters discussed in this section is included in a Monte Carlo analysis (along with other sources of uncertainty discussed later in this paper), with an aim to evaluate the impact of the current regulation and potential future regulations that are net environmentally beneficial, accounting for uncertainty.

Landing and Take-Off Measured Engine Data

In the certification process for commercial aircraft engines, manufacturers are required to report emissions as measured in four different modes of operation.

- 100% available thrust for 0.7 minutes (Take-Off)
- 85% available thrust for 2.2 minutes (Climb)
- 30% available thrust for 4.0 minutes (Approach)
- 7% available thrust for 26 minutes (Taxi) (ICAO, 2008)

The results are published in the EDB, which provides measured data-points where in-production and historical aircraft engines can be compared directly to the ICAO standards. Figure 1 shows the trend of recent engine certifications from EDB v25a in relation to the standards (ICAO, 2018). Engines with Twin Annular pre-Mixing Swirler (TAPS) or Technology for Advanced Low NO_x (TALON X) combustors in the EDB fall significantly below the standard compared to the rest of the population, and are highlighted in Figure 1. These new combustor technologies have reduced NO_x emissions without showing an increase in fuel burn.

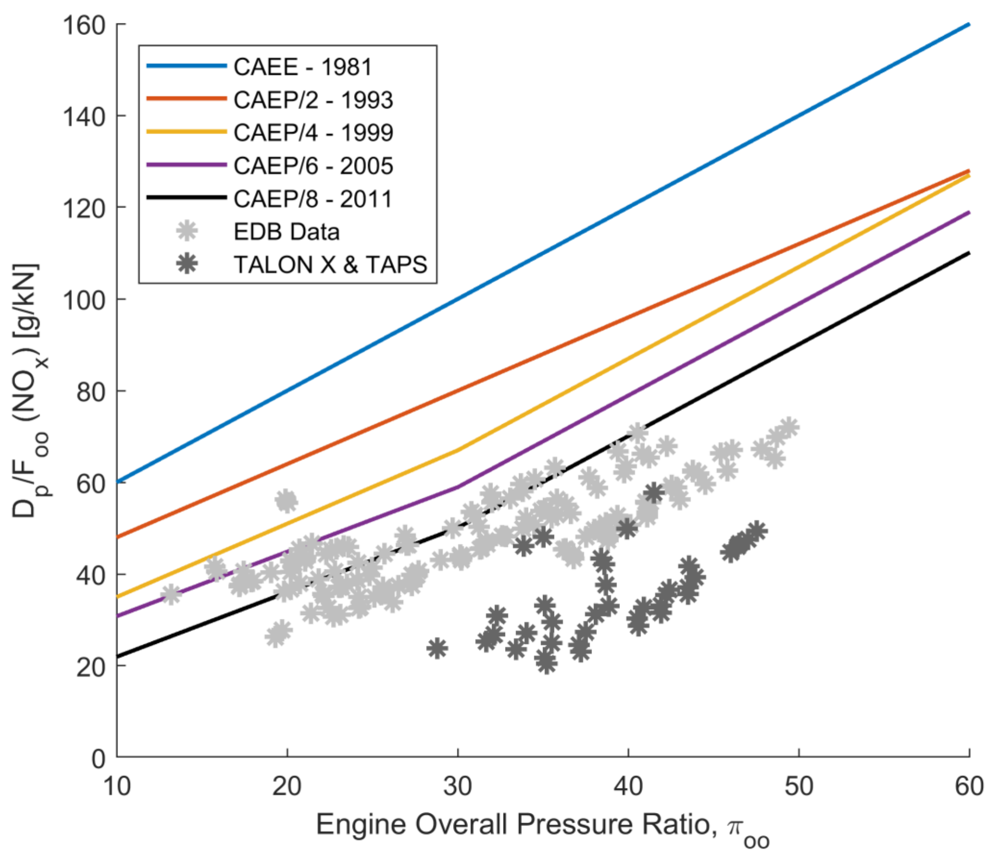

Figure 1: History of NO_x emissions standards per the Committee on Aircraft Engine Emissions and the Committee on Aviation Environmental Protection adopted by ICAO since 1981 compared to in-production aircraft data

Landing and Take-Off NO_x Emissions

Since this analysis aims to understand the allowable emissions per the current regulation, we consider hypothetical engines where LTO NO_x emissions match the level defined by the currently-applicable CAEP/8 (ICAO, 2008) regulation. This limit is defined as a function of OPR, given as

$$\frac{D_p(NO_x)}{F_{oo}} = \begin{cases} OPR \leq 30, & 7.88 + 1.4080\pi_{oo} \\ 30 < OPR \leq 62.5, & -9.88 + 2\pi_{oo} \\ OPR > 104.7, & 32 + 1.6\pi_{oo} \end{cases} \tag{1}$$

where the constants have units of g/kN. A history of each iteration of this regulation is included in Appendix A.

Landing and Take-Off CO_2 Emissions

CO_2 emissions for LTO operations are calculated based on measured fuel burn from the EDB. The emissions index (EI) of a species relates fuel burn to emission level, and is defined as a constant 3.155 kg CO_2 per kg of jet fuel. All in-production engines in the EDB are used to determine the relationship between total fuel burn in LTO as a function of engine OPR. Each of the four modes of operation (take-off, climb, approach, and taxi) are used in a time average, based on times in mode defined in the ICAO LTO cycle.

The best fit line for this relationship is determined to be

$$\frac{D_p(\mathrm{CO_2})}{F_{oo}} = 7233 + 29670\, e^{-0.0711\,\pi_{oo}} \tag{2}$$

where the constants have units of g/kN. The data, best fit and 95% confidence intervals are shown in Figure 2. In the Monte Carlo analysis, the 95% CI is used to define a triangular distribution about the best-fit line, based on residuals from the EDB data.

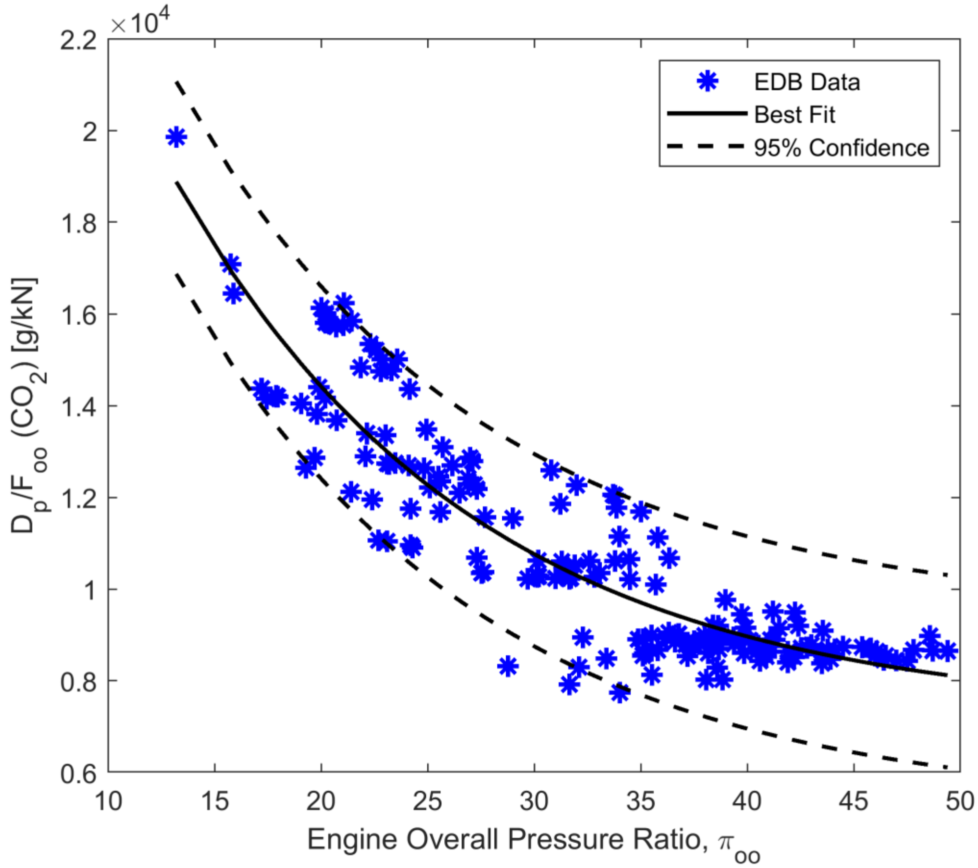

Figure 2: LTO CO_2 emissions as a function of reported OPR for all in-production engines in the ICAO EDB

Cruise NO_x Emissions

Without measurements from the EDB, estimates on aircraft fuel flow rates in cruise conditions must be made to determine cruise emissions. In reality, fuel flow rates change throughout the flight; even cruising at a constant speed and constant altitude requires varying thrust levels based on changing aircraft weight. AEIC is a tool used to estimate aircraft operating conditions over entire flights, and takes into account varying weights, varying thrust levels and varying segments of the flight (Simone et al., 2013). Although AEIC can be used in this analysis, the intention of this work is to evaluate the impacts of a regulation applied at engine certification, and therefore should not be flight path or aircraft specific. Therefore, other assumptions on an average and representative cruise fuel flow for each engine can be made, and the compared with AEIC as a form of validation.

Dimensional analysis is used to estimate cruise fuel flow with an energy balance. The rate of energy supplied by the fuel is represented in the numerator, while the denominator represents a rate of work (Cumpsty and Heyes, 2015). The sea level and cruise comparison is

$$\left.\frac{\dot{m}_f\ \mathrm{LCV}}{\sqrt{c_p\, T_{02}}\, D^2\, p_{02}}\right|_{\text{Sea Level}} = \left.\frac{\dot{m}_f\ \mathrm{LCV}}{\sqrt{c_p\, T_{02}}\, D^2\, p_{02}}\right|_{\text{Cruise}} \tag{3}$$

where D^2 is a characteristic diameter of the engine, and the lower calorific value (LCV) and specific heat (c_p) are characteristics of the fuel, therefore are constant between the same engine operating at two conditions. The simplified equation is

$$\frac{\dot{m}_{f_{\text{Cruise}}}}{\dot{m}_{f_{\text{Sea Level}}}} = \frac{p_{02,\text{Cr}}}{p_{02,\text{SL}}}\sqrt{\frac{T_{02,\text{Cr}}}{T_{02,\text{SL}}}} \tag{4}$$

Using the International Standard Atmosphere (ISA) at 35,000 ft to represent cruise and an assumed flight Mach number of 0.8, and using ISA at sea level and static conditions to represent sea level, isentropic flow equations are used to define the pressures and temperatures. The relationship is

$$\dot{m}_{f_{\text{Cruise}}} = 0.33\, \dot{m}_{f_{\text{Sea Level}}} \tag{5}$$

The resulting ratio shows that the fuel flow at cruise can be estimated as 33% of the fuel flow at sea level at an equivalent power level. When compared to AEIC data, discussed further below, sea level climb-out (85% thrust) can be used to represent cruise power levels. A detailed outline of this approach is included in Appendix B.

Using 69 known aircraft-engine pairs (listed in Appendix C), AEIC is used to validate cruise fuel flow from above. This list was compiled from active aircraft with engines listed in the EDB per AEIC source data. To minimize the variation associated with direct AEIC output, representative cruise conditions were chosen corresponding to the 3 gross weights used in the ICAO CO_2 standard. This simplifies the analysis by removing varying aircraft weight and fuel burn rates based on flight paths, airport pairings, and route distances. A high gross weight, mid-weight, and low gross weight representative of cruise are calculated based on reported maximum take-off mass (MTOM) (ICCT, 2013).

$$M_{\mathrm{Low}} = (0.45 \times \mathrm{MTOM}) + (0.63 \times (\mathrm{MTOM}^{0.924})) \tag{6}$$

$$M_{\mathrm{Mid}} = \frac{(M_{\mathrm{High}} + M_{\mathrm{Low}})}{2} \tag{7}$$

$$M_{\mathrm{High}} = 0.92 \times \mathrm{MTOM} \tag{8}$$

The agreement between the non-dimensional analysis and the AEIC output, shown in Appendix B, provides the basis for using a 33% scalar on sea level fuel flow to represent cruise fuel flow for the remainder of this analysis.

Once cruise fuel flow is known, the BFFM2 provides an extrapolation technique for emissions at altitude. Unlike CO_2, NO_x does not have a constant EI that ties it directly to fuel flow. The BFFM2 uses measured data from the EDB for each engine, applies corrections for installation and altitude effects, and uses a log-log extrapolation for determining the NO_x EI (Dubois et al., 2006; Baughcum et al., 1996). This method is outlined in more detail in Appendix D. Cruise altitude is assumed to be 7,000 ft below the aircraft ceiling, the same assumption used in AEIC (Simone et al., 2013). Implementing this technique across the 69 aircraft-engine combinations shows a trend between LTO NO_x emissions per rated thrust and average cruise emissions rate per rated thrust, shown in Figure 3.

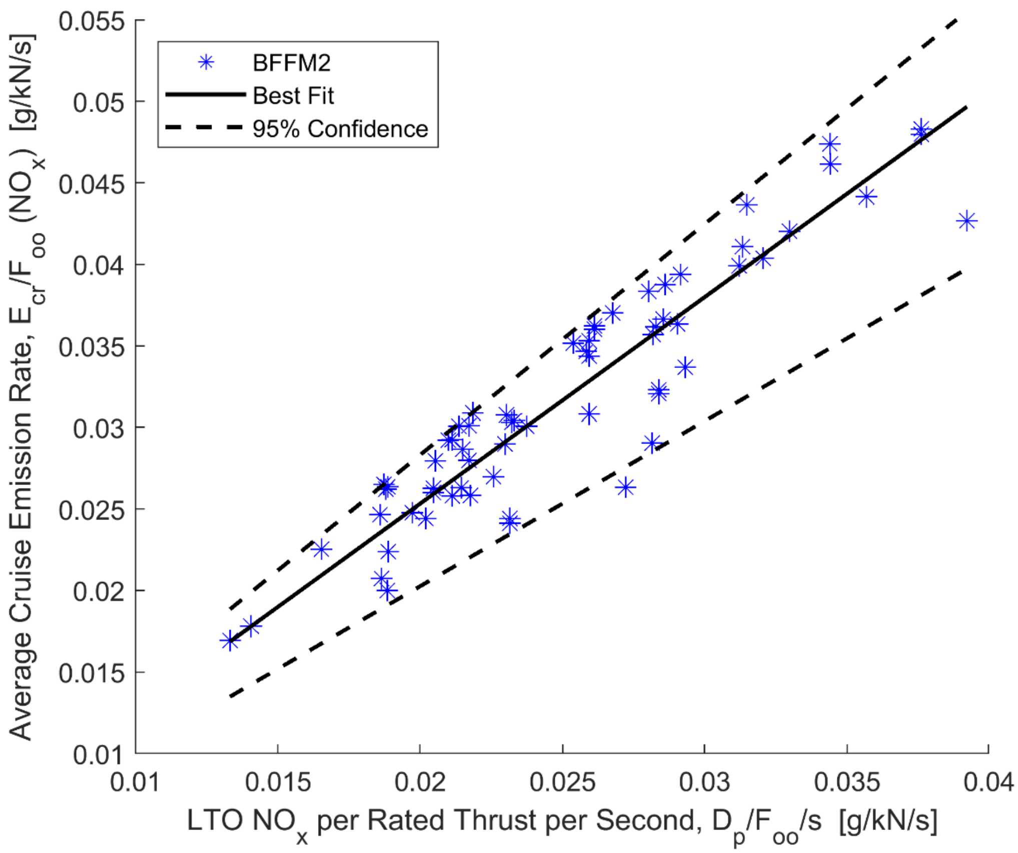

Figure 3: Average cruise NO_x emissions per unit rated thrust as a function of LTO NO_x for 69 AEIC aircraft-engine pairs

The best fit line is determined to be

$$\frac{\mathrm{ER_{cr}(NO_x)}}{F_{oo}} = 1.266 \times \left(\frac{D_p}{F_{oo}}\right)_{\mathrm{LTO}} \quad (9)$$

where the constants have units of g/kN/s and ER_{cr} is used to represent the emissions rate (per second) in cruise operation. To capture the uncertainty with this analysis, error bands capturing the 95% confidence interval have been added around the best fit line, with R^2 = 0.861. These bounds are included in the Monte Carlo analysis as a multiplied of the slope of this relationship.

Cruise CO_2 Emissions

Although a fuel flow rate was used in the previous section to extrapolate LTO NO_x emissions to cruise, that rate is not indicative of future engine technology. Therefore, to capture current and future technology and CO_2 emissions, engine cycle equations and representative technology values are used to develop a range of hypothetical engines across the engine design space.

Using gas turbine principles, an expression for net power can be used with isentropic relationships in the compressor and turbine to derive an expression for cycle efficiency with four assumptions. This analysis is outlined in Cumpsty and Heyes (2015), with a high-level review included here and more detailed analysis in Appendix E.

First, the net power is defined as the difference between power produced in the turbine and power used to drive the compressor. This simplified representation assumes net power is used for propulsion. The power supplied by an ideal compressor and produced by an ideal turbine is represented by the mass flow, temperature change across the component, and the specific heat of air. Then, an assumption for efficiency and isentropic equations can be substituted to represent real work.

Combining the definitions for turbine and compressor work yields an expression for cycle specific work. Simplified, it includes only four parameters: compressor efficiency, turbine efficiency, pressure ratio, and operating temperature ratio. Temperature ratio is defined as the ratio between the combustor exit temperature, the hottest point in the engine cycle, and the static inlet temperature. Using the same pressure ratio for both the compressor and turbine expressions assumes a negligible pressure drop across the combustor.

Specific work is then used to find an expression for cycle efficiency, represented as the ratio between the amount of power produced by the cycle (output), and the work done in the combustor (input), i.e.

$$\eta_{\mathrm{cycle}} = \left(\eta_{\mathrm{turb}} \frac{T_4}{T_2}\left(1 - \frac{1}{\mathrm{PR}^{\left(\gamma - \frac{1}{\gamma}\right)}}\right) - \frac{\mathrm{PR}^{\left(\gamma-\frac{1}{\gamma}\right)} - 1}{\eta_{\mathrm{comp}}}\right)\left(\frac{T_4}{T_2} - \left(1 + \frac{\mathrm{PR}^{\gamma-\frac{1}{\gamma}} - 1}{\eta_{\mathrm{comp}}}\right)\right)^{-1} \quad (10)$$

Thrust can be calculated from the fuel flow, overall efficiency (combining cycle and propulsive efficiency), velocity and fuel heating value as

$$F = \frac{\eta_{\mathrm{overall}}\, W_f\, \mathrm{LHV}}{\mathrm{Velocity}} \quad (11)$$

Rated thrust can be assumed from a known lapse rate in air density. Finally, rated thrust and the emissions index of CO_2 can be used to estimate cruise emissions per rated thrust per second of flight without an explicit assumption on fuel flow, defined as

$$\frac{\mathrm{ER_{cr}(CO_2)}}{F_{oo}} = \frac{\mathrm{EI_{CO_2}}}{\mathrm{LR}\left[\left(\eta_{\mathrm{cycle}} \times \eta_{\mathrm{prop}}\right) \mathrm{LHV} / \ \mathrm{Velocity}\right]} \quad (12)$$

To represent current engine technology and future engine technology, a range of each of the above assumptions are made and listed in Table 1. These ranges are chosen based on representative values with input from industry experts. These values are used in the Monte Carlo analysis to estimate cruise CO_2 emissions as a function of OPR.

Figure 4 shows the 95% confidence interval for CO_2 emissions at cruise based on the assumptions for component efficiencies, temperature ratio, and propulsive efficiency. Additionally, for validation, output from representative engine cycle models provided by a major gas turbine manufacture have been included. The red data represents 1990's technology, while the blue data represents a 2010's engine.

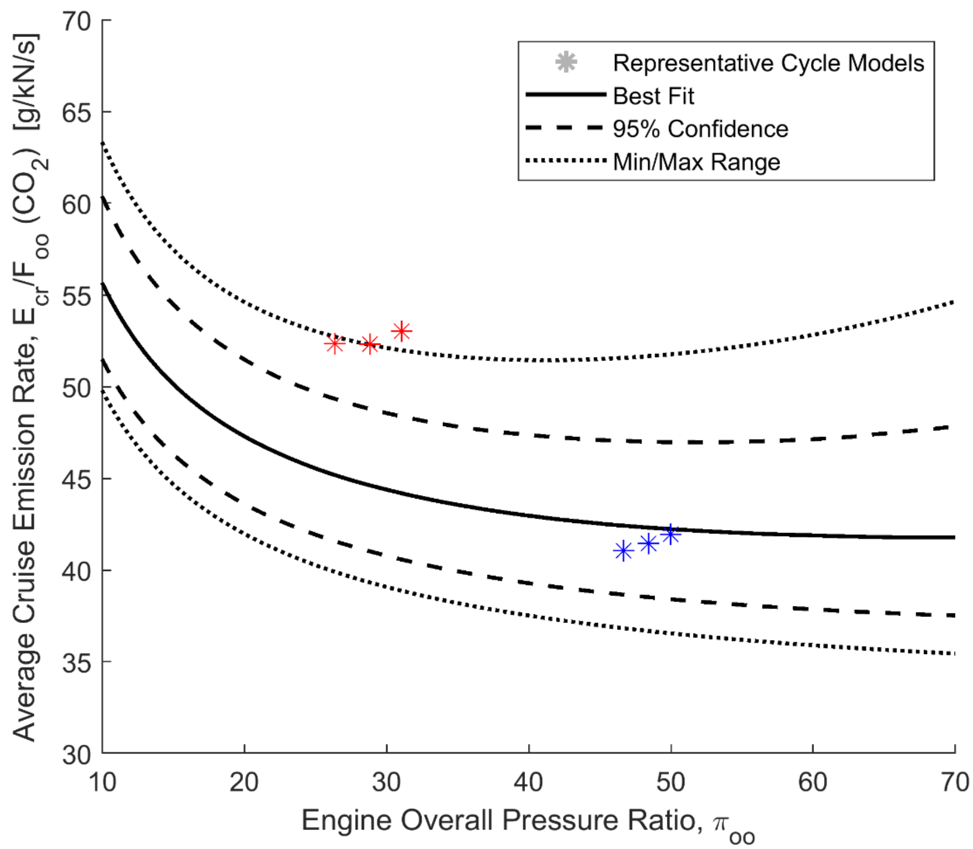

Figure 4: Cruise CO_2 emissions as a function of OPR with two representative cycle models at three high power settings included for reference

<u>Climate and Air Quality Environmental Damages</u>

Once all four unknown emission rates are estimated across a range of OPRs, the impacts of those emissions are quantified. In this analysis, the social cost of engine operation considers the marginal cost of fuel production, and climate and air quality damages associated with emissions.

RF impacts from NO_x are attributed to four pathways: short lived O_3 production, long term O_3 depletion, long term CH_4 depletion, and nitrate aerosol formation. Additionally, NO_x

contributes to local air quality damage via $PM_{2.5}$ and O_3 production. CO_2 is a greenhouse gas and therefore directly impacts climate and RF, but is not considered in our air quality analysis.

Grobler et al. (2019) describes the pathways, climate and air quality impacts for each emissions species, and monetizes those impacts with uncertainty bounds. Each damage value is presented in US dollars per tonne of emissions species. Appendix F contains values and 95% confidence intervals for each pathway, for multiple discount rates. Including only these impacts provides an environmental cost basis for regulating aviation NO_x emissions, but a further social cost is also considered.

Marginal Production Cost of Fuel

Fuel consumption is also included in quantifying the social costs of engine operation. While the market price of jet fuel represents a transfer that does not constitute a social cost, the production of fuel consumes resources that could be expended elsewhere. Therefore, the marginal cost of jet fuel production is included in the social cost metric, which is computed from the market price of jet fuel and markup rates from the literature. Khan et al. (2013) showed oil price markup between the years 1980 and 2010 ranged from 4.45 to 4.75. Considine (2001) presents a Lerner Index of 62.3%, 43.3%, and 45.9% for jet fuel, which is equivalent to a 2.65, 1.76, and 1.84 markup respectively.

Using historical data from ThomsonOne (JETA Y-IL) to find the price of jet fuel for 2013-2018, and the markup rates from above, the marginal production cost of a unit of jet fuel can be estimated for a 5 year period. The Lerner Index and historical price of Jet A are described in more detail in Appendix G.

Costs per Unit Operating Time

A weighted-average of emission rates is found based on the time a flight spends between cruise and LTO operation. Short-haul flights have a higher percentage of LTO operation, while long-haul flights are heavily weighted towards cruise.

Examining the global 2013 AEIC flight inventory, the average cruise operation was found to account for 73.2% of total flight time, with a minimum of 9.1% and a maximum of 95.2%. This is based on an LTO cycle of 2,897 s (0.8 hr) as outlined in Settler et al. (2011), which matches the assumption used while developing AEIC. This is considered more representative of actual operations than the ICAO cycle. The distribution of flight times is included in Appendix H for reference.

Finally, to calculate the LTO and cruise operation costs, the following equations are used with emissions per rated thrust per second of operation, the marginal cost of fuel, and the damage distributions from Grobler et al. (2019).

Nominal values for each of the above analyses are used to calculate a set of nominal results, and are listed in Table 1. Combined social costs are presented as a function of OPR, and are discussed in the first section of results.

Next, Sobol sequences are used to combine all the previous uncertainty, which mathematically sample the desired distribution shapes uniformly (Sobol et al., 2001). A Monte Carlo analysis with 10,000 cases is performed, and used to evaluate the allowable social costs per the current CAEP/8 limit. Distributions from individual emission sources are shown in Appendix I, while the distributions from environmental damage pathways are shown in Appendix J.

Finally, alternate NO_x limits are evaluated and compared to the current regulation. Specifically, the mid- and long-term goals set by ICAO's Working Group 3, and a case where social costs are constant across the OPR range. These studies use the 10,000 Monte Carlo runs.

Table 1: Summary of Nominal Values and Monte Carlo Distributions

Source	Units	Nominal	Shape	Defining Parameters	
Emission Distributions					
NO_x Cruise Emissions	g/kN/s	Equation (8)	Triangular	Median: Equation (8)	L = 0.85, M = 0.925, U = 1.3
Temperature Ratio	-	6.0	Uniform	Lower Bound: 5.5	Upper Bound: 7.0
Compressor Efficiency	-	85% Adiabatic	Uniform	Lower Bound: 0.89	Upper Bound: 0.915
Turbine Efficiency	-	95% Adiabatic	Uniform	Lower Bound: 0.88	Upper Bound: 0.93
Propulsive Efficiency	-	75%	Uniform	Lower Bound: 0.7	Upper Bound: 0.8
CO_2 LTO Emissions	g/kN	Equation (2)	Triangular	Median: Equation (2)	L = -0.4, M = 0.0, U = 0.4
Time in Cruise	seconds	7,900	Triangular	L = 900 M = 4,000 U = 54,000	
Damage Distributions					
Marginal Cost of Fuel	\$/tonne CO_2	45	Triangular	L = 22.3, M = 68.1, U = 195	
NO_x Climate Damage: Cruise	\$/tonne NO_x	-940	Per Figure A-24	95% Confidence Interval [-2600, -120]	
NO_x Climate Damage: LTO	\$/tonne NO_x	-590	Per Figure A-25	95% Confidence Interval [-1600, -81]	
CO_2 Climate Damage: Cruise	\$/tonne CO_2	45	Per Figure A-26	95% Confidence Interval [6.7, 120]	
CO_2 Climate Damage: LTO	\$/tonne CO_2	45	Per Figure A-27	95% Confidence Interval [6.7, 120]	
NO_x Air Quality Damage: Cruise	\$/tonne NO_x	21,000	Per Figure A-22	95% Confidence Interval [3700, 67000]	
NO_x Air Quality Damage: LTO	\$/tonne NO_x	26,000	Per Figure A-23	95% Confidence Interval [4600, 82778]	

Note: L, M and U represent the lower, middle and upper characteristics for a triangular distribution.

Results

First, results from the nominal analysis are shown, followed by a Monte Carlo analysis.

Costs per Unit Operating Time: Nominal

Using nominal values from Table 1, Figure 5 shows the tradeoff between the NO_x and CO_2 emissions rate per rated thrust from cruise and LTO operation as a function of OPR, with contours of constant social cost. This shows that as OPR is increased, the social cost decreases initially, reaches a minimum, and then begins to climb again. For consistency, the difference between the constant social cost contours in LTO and cruise is the same magnitude ($5x10^{-4}$ $/s/kN), but have different slopes because the two modes of operation have different damages associated with the emissions. All values shown in these results reflect a discount rate of 3%.

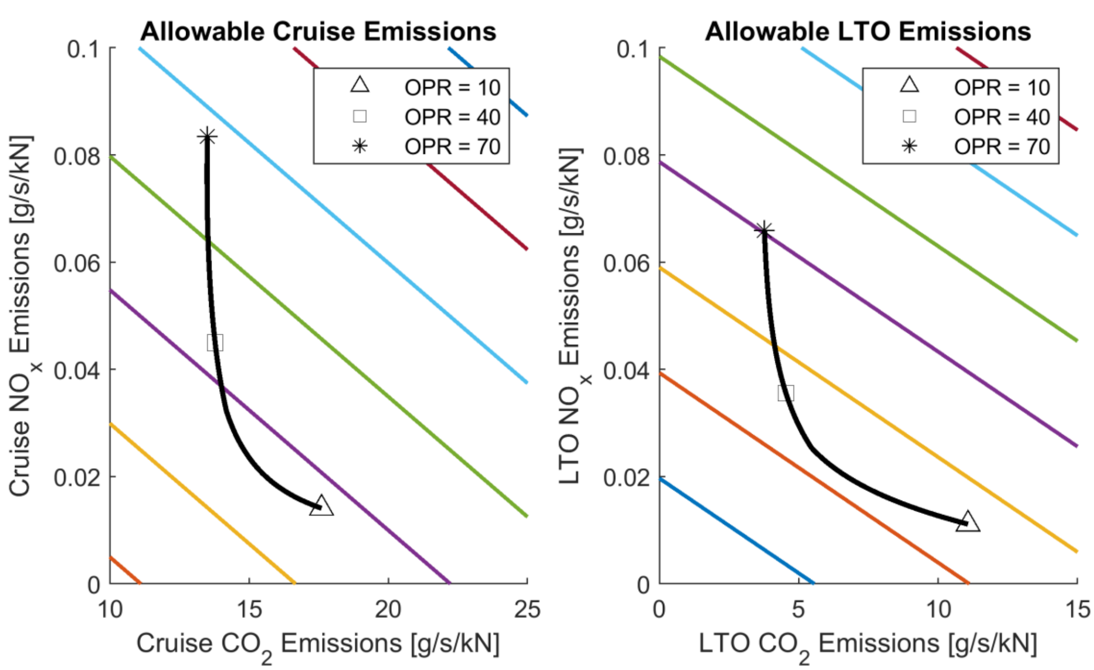

Figure 5: NO_x and CO_2 emissions for a range of OPRs (10 to 70) with lines of constant social costs in cruise and LTO respectively for reference

Figure 6 shows the resulting damages associated with climate, air quality, and marginal cost of fuel broken down into their respective contributions. The shape of the overall social cost displays a minimum point that occurs approximately at an OPR of 20, and biases at the high and low OPRs where social costs are higher. This implies the regulation as it is defined today allows for an uneven distribution of social cost across the design space. Climate damages and fuel costs make-up the majority of combined social cost at lower OPR, while air quality damage from NO_x makes-up the majority at higher OPR. This trend is especially important to understand as newer engines move to higher OPR values.

As OPR is increased, near-constant values for the climate and fuel cost terms reflect the diminishing returns in efficiency, while the CAEP/8 regulation shape allows the contributions from air quality to climb. The near-constant fuel cost contribution also demonstrates the trends from an environmental cost basis (with climate and air quality contributions only) and a social cost basis are similar.

This analysis and the emissions tradeoffs shown are not necessarily indicative of thermodynamic tradeoffs in the physics of gas turbine engines; this is only an analysis on allowable emissions per the currently-applicable CAEP/8 standard. For example, higher NO_x emissions shown here do not require higher temperatures; they are a product of the regulation being defined as a function of OPR. Furthermore, the minimum in damages at an OPR of 20 does not imply that this is an environmentally optimal engine design for all engines; it is a product of the regulation as it is currently defined.

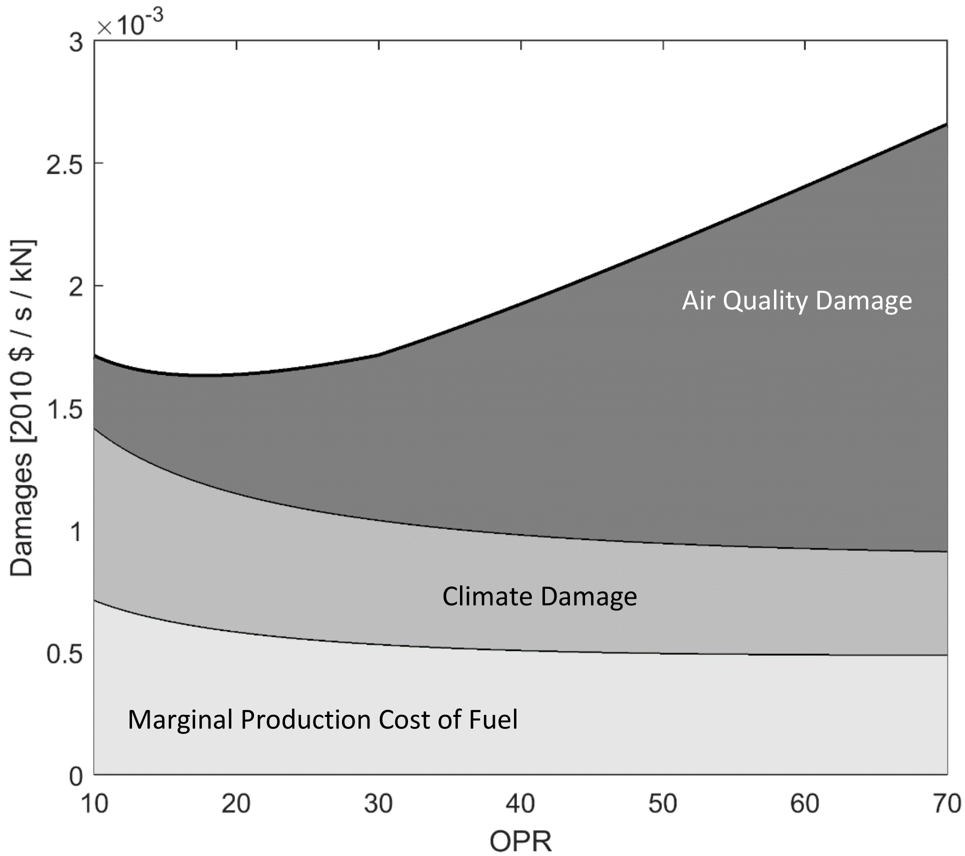

Figure 6: Nominal social cost analysis broken into marginal production cost of fuel, climate damage and air quality damage

Costs per Unit Operating Time: Monte Carlo

The distribution of total social costs per second of operation for operations at the level of the CAEP/8 standard is shown in Figure 7 with the median, 50%, and 95% confidence intervals drawn. These results also show that there is an uneven distribution of damage over the engine design space, where going to higher OPRs allows total environmental damage to increase. The distribution of OPRs at which minimum damage occurs is shown in Figure 8.

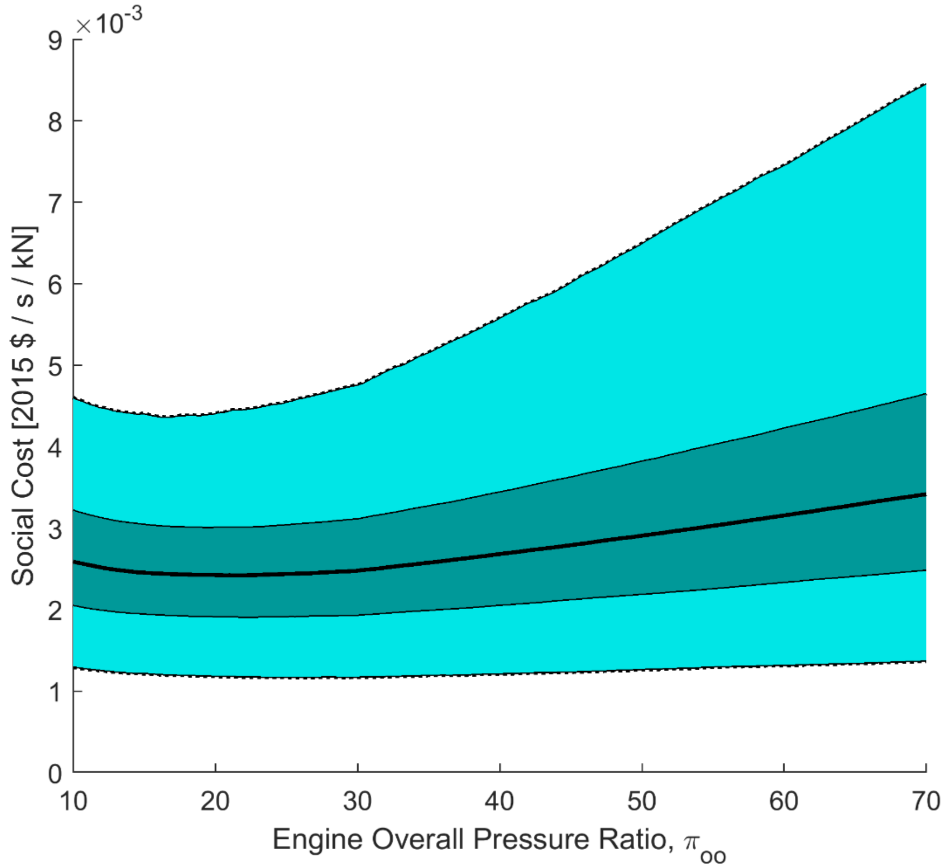

Figure 7: Distribution of combined environmental and social costs per rated thrust per second of operation, allowable per the CAEP/8 limit

A breakdown of Figure 7 into climate damage, air quality damage, and the marginal cost of fuel as a function of OPR for LTO and cruise separately is shown in Appendix K. Climate damages and fuel costs make up the majority of combined social cost at lower OPR, while air quality damage from NO_x make up the majority at higher OPR.

A sensitivity analysis is also conducted for these results, breaking out the uncertainty contributions from each of the inputs listed in Table 1. The distribution of monetized environmental damages associated with emission levels per Grobler et al. (2019) account for ~80% of the uncertainty at an OPR of 40. Full results are listed in Appendix L.

Figure 8 shows the empirical cumulative distribution function at which OPR of minimum social costs occur for each of the 10,000 Monte Carlo simulations. This figure shows 50% of simulations have social cost climbing by an OPR of 22, and 90% of Monte Carlo cases have social cost climbing by an OPR of 36. These results show that new engines, which are higher OPR designs, have higher allowable social costs than previous lower OPR engine designs, if they operate near the CAEP/8 NO_x limit.

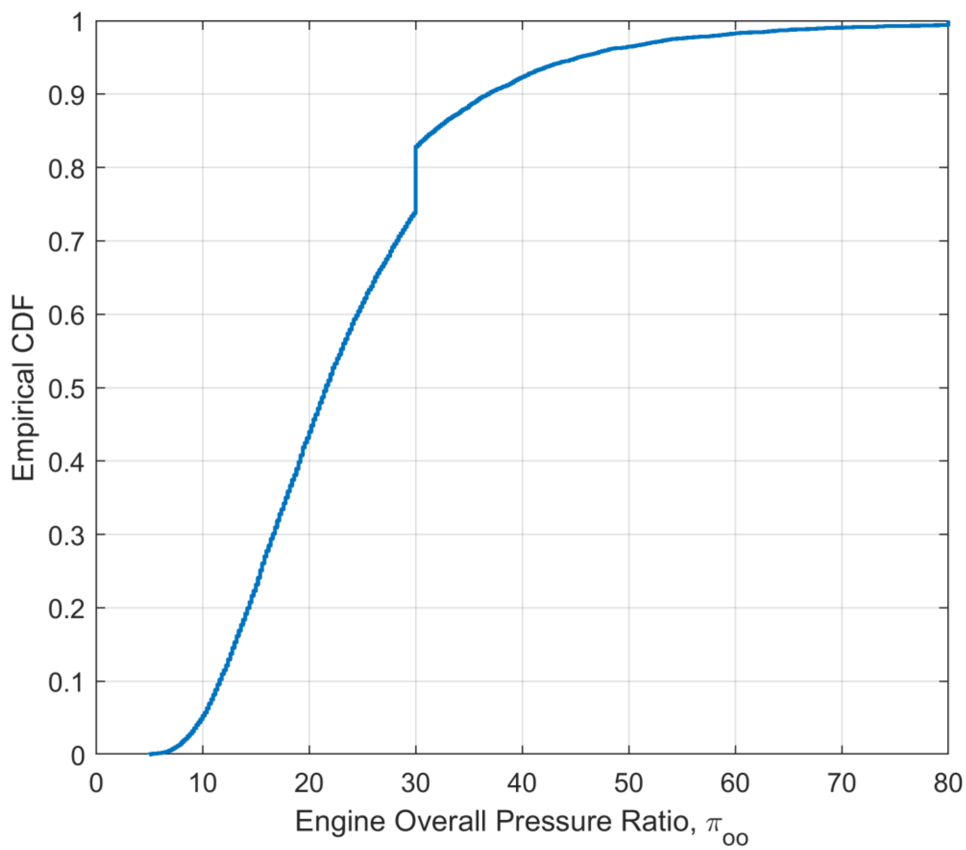

Figure 8: Distribution of OPR associated with minimum social cost showing a bias towards low OPR engine design and an OPR of 30, where the current regulation changes slope

With 10,000 runs in the Monte Carlo analysis, a new trend also becomes obvious: as a result of the regulation changing slope at an OPR of 30, there is a biased minimum damage point. This can be seen in Figure 8 as a step change at an OPR of 30.

In 2007, ICAO also announced mid- and long-term goals for NO_x emissions, for the years 2016 and 2026 respectively. These are shown on Figure 9 as dotted lines, and are defined as a 45% and 60% reduction at an OPR of 30 from the CAEP/6 standards (Dickson, 2015).

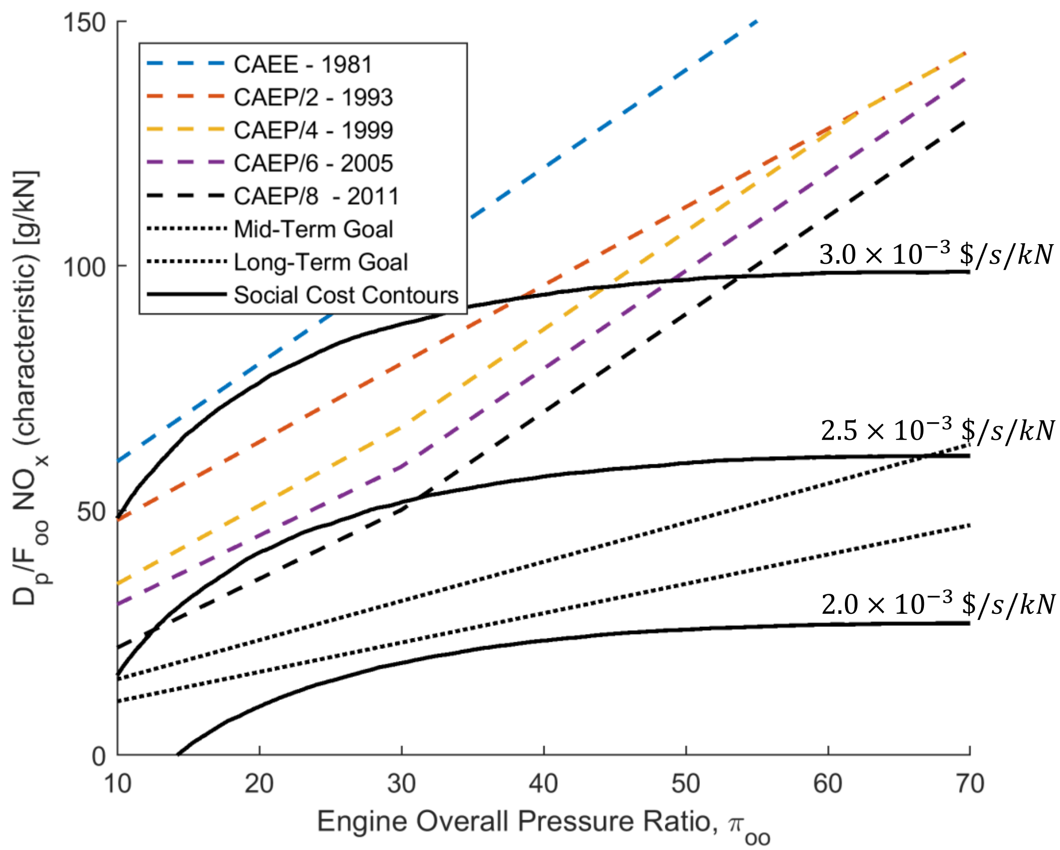

Figure 9: Comparison of historical ICAO standards, ICAO goals, and constant social cost contours

For comparison, the total allowable social costs from hypothetical engines operating at those emission levels are displayed in Figure 10, and show a more even distribution of social costs across engine OPR on the same cost-scale as compared to Figure 7. CAEP/8 results are shown in grey with dashed lines in the background for reference, and results from the mid- and long-term goals are shown in teal.

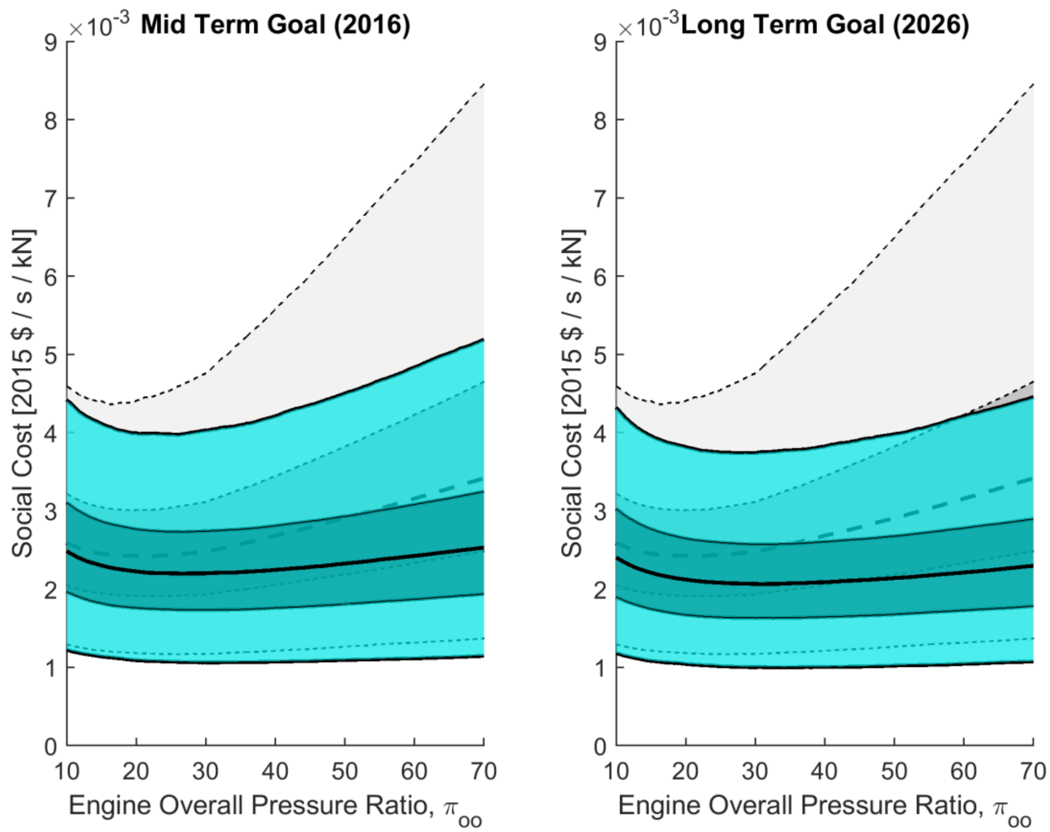

Figure 10: Social costs of NO_x emissions at the levels of the ICAO mid-term and long-term goals, with CAEP/8 results shown in the background for reference

Finally, instead of assuming new definitions of the standard will be based on previous versions, an alternative approach to defining the NO_x standard is evaluated in an effort to reduce the trends in total allowable damage. The solid black lines shown in Figure 9 represent lines of constant social cost, and are defined with the goal of removing the OPR bias in the 50^{th} percentile of the Monte Carlo runs.

Comparing the results from the ideal constant social cost analysis to the mid- and long-term goals set by CAEP shows the benefit of moving towards those goals from the current definition. By scaling previous versions of the regulation down at all OPRs, instead of a constant reduction, the social cost is more even across the design space.

The overall social cost for the mid-contour shown in Figure 9 is displayed in Figure 11. The 50th percentile range is now constant across OPR, and when compared to the original results, the absolute range of damages is smaller than before.

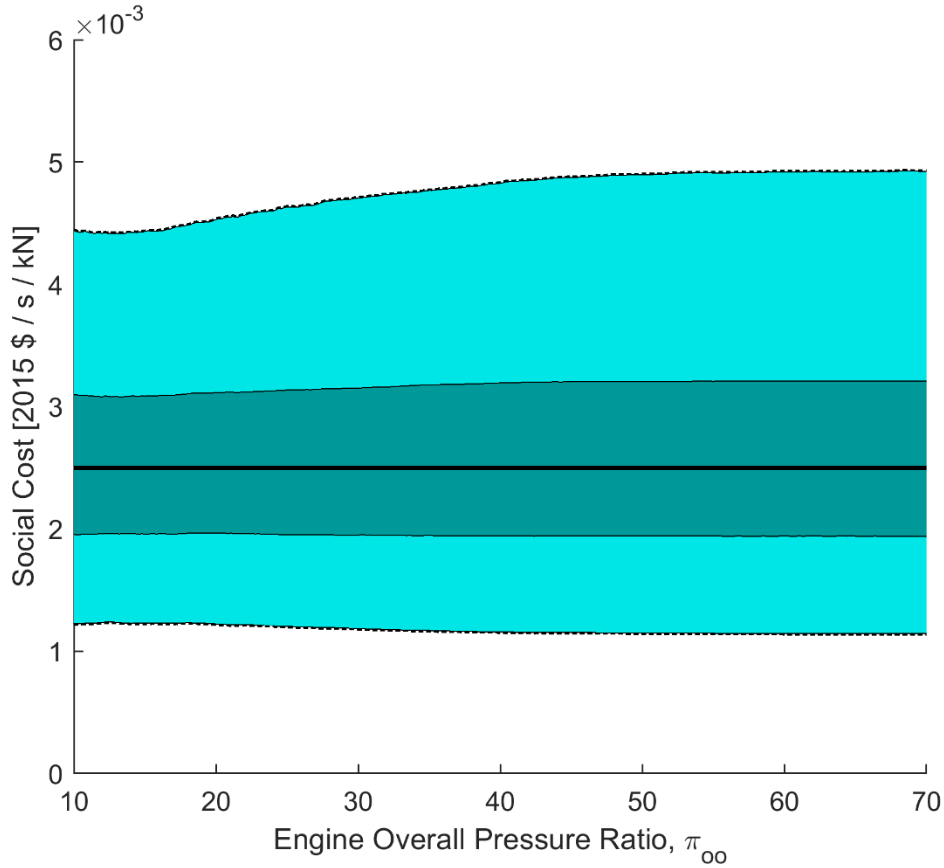

Figure 11: Total allowable combined environmental and social cost from a constant social cost contour

Conclusions

Using the environmental or social cost basis derived in this thesis for NO_x regulations would encourage engine manufacturers to employ technology to reduce NO_x emissions. A NO_x standard defined on this basis, with combustor technology that can achieve a set level of NO_x emissions as a function of OPR, would yield an intersection of two curves that defines the maximum OPR that could be used with the given technology while meeting the standard. If combustor technology is improved to further reduce NO_x emissions, this intersection will move to higher OPR, allowing an increase in engine efficiency while holding social costs constant. Thus, a NO_x standard designed in this way provides incentives for development of improved technologies for minimizing NO_x emissions, since doing so would allow manufacturers to build more fuel-efficient engines which are also more attractive to their customers.

This research could be taken a step further to suggest NO_x regulations should not be defined as a function of OPR at all, but instead defined as a function of SFC. Since OPR is used as a way to determine CO_2 emissions in this work, it makes sense that CO_2 emissions (and therefore fuel flow rates) could be used directly.

A challenge of using a social cost analysis for actually setting regulatory limits is that the inputs are subject to change over time. Fuel costs can change rapidly with market fluctuations, new engine technology is developed, and impacts from emissions change as background levels change. Considering the multi-decade lifespan of an aircraft engine certified for a particular NO_x standard, the social cost estimates applicable to that engine should be developed with damages applicable to these future times in mind.

Another aspect of this research with high uncertainty is how to monetize damages. All primary results are shown with a discount rate of 3%. Since CO_2 is a long-term greenhouse gas, low discount rates increase the relative contribution of CO_2 damage in this analysis, while short term air quality impacts are valued more highly with high discount rates. Results for 2% and 7% discount rates are included in Appendices N and O, respectively. Results show that higher discount rates diminish the overall costs, but lower discount rates are more constant across the range of OPRs from reducing the NO_x air quality damage that dominates at high OPR.

This research could also be improved with more reliable emissions data at altitude. Several campaigns have been performed to capture emissions data, but the uncertainty levels are too high to use here. Additionally, these campaigns have been done on only a handful of aircraft, and therefore cannot be used to represent the world-wide fleet. Without cruise emission data widely available this analysis relies upon several different calculation and extrapolation techniques. One solution would be to require manufactures to report cruise-equivalent points in certification (like the EDB exists for LTO). Research shows cruise operation makes up the majority of aviation related air quality and climate impacts, therefore understanding those emission rates is critical to being able to evaluate impacts accurately.

Despite these unknowns and challenges, this thesis demonstrates a new way to evaluate current and proposed regulations, by demonstrating why a holistic approach is needed to fully understand and quantify the environmental impacts associated with regulations.

References

[1] S. H. Yim, G. L. Lee, I. H. Lee, F. Allroggen, A. Ashok, F. Caiazzo, S. D. Eastham, R. Malina and S. R. Barrett, "Global, regional and local health impacts of civil aviation emissions," *Environmental Research Letters,* vol. 10, no. 3, 2015.

[2] The Boeing Company, "Commercial Market Outlook 2018-2037," 2018.

[3] M. E. Stettler, S. Eastham and S. R. Barrett, "Air quality and public health impacts of UK airports. Part I: Emissions," *Atmospheric Environment,* pp. 5415-5424, 2011.

[4] I. M. Sobol and S. S. Kucherenko, Global sensitivity indices for nonlinear mathematical models, John Wiley & Sons Ltd., 2007, pp. 164-167.

[5] N. W. Simone, M. E. Stettler and S. R. Barrett, "Rapid estimation of global civil aviation emissions with uncertainty quantification," *Transportation Research Part D: Transport and Environment,* vol. 25, pp. 33-41, 12 2013.

[6] D. S. Lee, D. W. Fahey, P. M. Forster, P. J. Newton, R. C. Wit, L. L. Lim, B. Owen and R. Sausen, "Aviation and global climate change in the 21st century," *Atmospheric Environment,* pp. 3520-3537, 2009.

[7] K. G. Kyprianidis and E. Dahlquist, "On the trade-off between aviation NO_x and energy efficiency," *Applied Energy,* vol. 185, pp. 1506-1516, 2017.

[8] K. Kundu, P. Penko and S. Yang, "Simplified Jet-A/air combustion mechanisms for calculation of NO_x emissions," American Institute of Aeronautics and Astronautics (AIAA), 2018.

[9] H. Khan and B. G. Kim, "Markups and oil prices in Canada," *Economic Modelling,* pp. 799-813, 2013.

[10] International Counsel on Clean Transportation, "ICAO CO2 Certification for New Aircraft," in *ICCT Policy Update*, 2013.

[11] International Civil Aviation Organization, "Annex 16 to the Convention on International Civil Aviation. Environmental Protection. Volume II. Aircraft Engine Emissions. Third Edition," 2008.

[12] International Civil Aviation Organization, "Aircraft Engine Emissions Databank v25a," 2018.

[13] C. Grobler, P. Wolfe, K. Dasadhikari, I. Dedoussi, F. Allroggen, R. L. Speth, S. D. Eastham, A. Agarwal, M. D. Staples, J. Sabnis and S. R. H. Barrett, "Marginal Climate and Air Quality Costs of Aviation Emissions," *Forthcoming,* 2019.

[14] S. Freeman, D. S. Lee, L. L. Lim, A. Skowron and R. R. De León, "Trading off Aircraft Fuel Burn and NO_x Emissions for Optimal Climate Policy," *Environmental Science and Technology,* pp. 2498-2505, 2018.

[15] S. D. Eastham and S. R. Barrett, "Aviation-attributable ozone as a driver for changes in mortality related to air quality and skin cancer," *Atmospheric Environment,* pp. 17-23, 2016.

[16] N. Dickson, "Local Air Quality and ICAO Engine Emissions Standards," ICAO, 2015.

[17] N. Cumpsty and A. Heyes, Jet Propulsion, 3rd edition, Cambridge University Press, 2015, pp. 102-103.

[18] T. J. Considine, "Markup pricing in petroleum refining: A multiproduct framework," *International Journal of Industrial Organization,* pp. 1499-1526, 2001.

[19] S. L. Baughcum, T. G. Tritz, S. C. Henderson and D. C. Pickett, "Scheduled Civil Aircraft Emission Inventories for 1992: Database Development and Analysis," 1996.

[20] S. R. H. Barrett, R. E. Britter and I. A. Waitz, "Global mortality attributable to aircraft cruise emissions," *Environmental Science and Technology,* vol. 44, no. 19, pp. 7736-7742, 1 10 2010.

[21] D. Dubois and G. C. Paynter, "Fuel Flow Method 2 for Estimating Aircraft Emissions," The Boeing Company, SAE International, 2006.

Appendices

A. History of CAEP NO_x Regulations

Per Annex 16 to the Convention on International Civil Aviation, Volume 2 Aircraft Engine Emissions, the following emissions standards for NO_x apply to subsonic commercial aircraft.

- For engines of a type or model for which the date of manufacture of the first individual production model was before 1 January 1996 and for which the date of manufacture of the individual engine was before 1 January 2000:

$$\frac{D_p}{F_{oo}} = 40 + 2\pi_{oo}$$

- For engines of a type or model for which the date of manufacture of the first individual production model was on or after 1 January 1996 or for which the date of manufacture of the individual engine was on or after 1 January 2000:

$$\frac{D_p}{F_{oo}} = 32 + 1.6\pi_{oo}$$

- For engines of a type or model for which the date of manufacture of the first individual production model was on or after 1 January 2004:

   - $For\ F_{oo} > 89.0\ kN$

$$\frac{D_p}{F_\infty} = \begin{cases} \text{OPR} \leq 30, & 19 + 1.6\pi_{oo} \\ 30 < \text{OPR} \leq 62.5, & 7 + 2\pi_{oo} \\ \text{OPR} > 62.5, & 32 + 1.6\pi_{oo} \end{cases}$$

   - $For\ 26.7\ kN < F_{oo} < 89.0\ kN$

$$\frac{D_p}{F_\infty} = \begin{cases} \text{OPR} \leq 30, & 37.572 + 1.6\pi_{oo} - 0.2087F_{00} \\ 30 < \text{OPR} \leq 62.5, & 42.71 + 1.4286\pi_{oo} - 0.4013F_{00} + 0.00642\pi_{oo}xF_{00} \\ \text{OPR} > 62.5, & 32 + 1.6\pi_{oo} \end{cases}$$

- For engines of a type or model for which the date of manufacture of the first individual production model was on or after 1 January 2008 or for which the date of manufacture of the individual engine was on or after 1 January 2013:
  - $For\ F_{oo} > 89.0\ kN$

$$\frac{D_p}{F_\infty} = \begin{cases} \text{OPR} \leq 30, & 16.72 + 1.4080\pi_{oo} \\ 30 < \text{OPR} \leq 62.5, & -1.04 + 2\pi_{oo} \\ \text{OPR} > 82.6, & 32 + 1.6\pi_{oo} \end{cases}$$

  - $For\ 26.7\ kN < F_{oo} < 89.0\ kN$

$$\frac{D_p}{F_\infty} = \begin{cases} \text{OPR} \leq 30, & 38.5486 + 1.6823\pi_{oo} - 0.2453F_{00} - 0.00308\pi_{oo}xF_{00} \\ 30 < \text{OPR} \leq 62.5, & 46.16 + 1.4286\pi_{oo} - 0.5303F_{00} + 0.00642\pi_{oo}xF_{00} \\ \text{OPR} > 82.6, & 32 + 1.6\pi_{oo} \end{cases}$$

- For engines of a type or model for which the date of manufacture of the first individual production model was on or after 1 January 2014:
  - $For\ F_{oo} > 89.0\ kN$

$$\frac{D_p}{F_\infty} = \begin{cases} \text{OPR} \leq 30, & 7.88 + 1.4080\pi_{oo} \\ 30 < \text{OPR} \leq 62.5, & -9.88 + 2\pi_{oo} \\ \text{OPR} > 104.7, & 32 + 1.6\pi_{oo} \end{cases}$$

  - $For\ 26.7\ kN < F_{oo} < 89.0\ kN$

$$\frac{D_p}{F_\infty} = \begin{cases} \text{OPR} \leq 30, & 40.052 + 1.5681\pi_{oo} - 0.3615F_{00} - 0.0018\pi_{oo}xF_{00} \\ 30 < \text{OPR} \leq 62.5, & 41.9435 + 1.505\pi_{oo} - 0.5823F_{00} + 0.005562\pi_{oo}xF_{00} \\ \text{OPR} > 104.7, & 32 + 1.6\pi_{oo} \end{cases}$$

B. Dimensional Analysis for Estimating Cruise Fuel Flow

A dimensional analysis is used to find the relationship between fuel flows for two flight conditions from the same engine, in this case cruise and LTO. From Cumpsty and Heyes (2015), the relationship is

$$\left.\frac{\dot{m}_f \text{ LCV}}{\sqrt{c_p\, T_{02}}\, D^2\, p_{02}}\right|_{\text{Sea Level}} = \left.\frac{\dot{m}_f \text{ LCV}}{\sqrt{c_p\, T_{02}}\, D^2\, p_{02}}\right|_{\text{Cruise}}$$

where

$$\text{Non} - \text{Dimensional Fuel Flow Rate} = \frac{\dot{m}_f \text{ LCV}}{\sqrt{c_p\, T_{02}}\, D^2\, p_{02}}$$

and D^2 (diameter) is a characteristic of the engine, and LCV (lower calorific value of fuel) and c_p (specific heat at constant pressure) are characteristics of the fuel, therefore are constant between two engine operating conditions. The simplified equation is

$$\left.\frac{\dot{m}_f}{\sqrt{T_{02}}\;\, p_{02}}\right|_{\text{Sea Level}} = \left.\frac{\dot{m}_f}{\sqrt{T_{02}}\;\, p_{02}}\right|_{\text{Cruise}}$$

Ambient conditions are assumed to match atmospheric standard day, shown below.

Sea Level:

- Ts = 288.15 K
- Ps = 101,325 Pa
- Mach = 0.0

Cruise, 35,000 ft:

- Ts = 218.8 K
- Ps = 23,800 Pa
- Mach = 0.8

Using Mach number to get stagnation properties from the above static assumptions, and rearranging the equation above, a ratio between cruise and LTO conditions is expressed as

$$\frac{\dot{m}_{f_{\text{Cruise}}}}{\dot{m}_{f_{\text{Sea Level}}}} = \left[\frac{p_{02,\text{Cr}}}{p_{02,\text{TO}}}\sqrt{\frac{T_{02,\text{Cr}}}{T_{02,\text{TO}}}}\right]$$

where pressures are in kPa and temperatures are in R. The resulting ratio is

$$\dot{m}_{f_{\text{Cruise}}} = 0.33\, \dot{m}_{f_{\text{Sea Level}}}$$

Climb-out (85% thrust) from the EDB is used to represent an equivalent power level at cruise, and therefore 33% of reported fuel flow in the EDB is used as cruise fuel flow. It is compared to fuel flow reported by AEIC in Figure A-12 below.

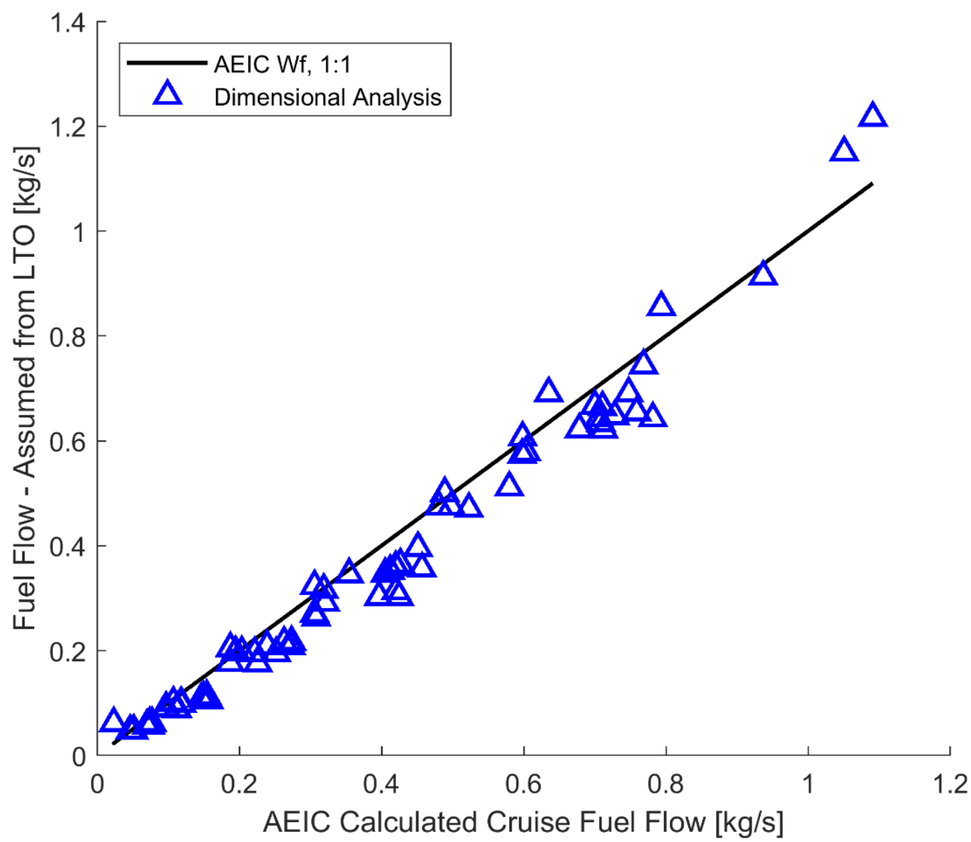

Figure A-12: Cruise fuel flow as estimated with dimensional analysis compared to reported fuel flow from AEIC, with an R^2 value of 0.9615

C. AEIC Aircraft-Engine List

Table A-2: AEIC Aircraft-Engine Pairs and EDB Matches

- AEIC V3.0 Database -		- Emissions Data Bank V25a -	
AEIC Aircraft	AEIC Engine	EDB Match	UID No
A306	PW4158	PW4158	1PW048
A30B	CF6-50C2	CF6-50C2	3GE074
A310	CF6-80C2A2	CF6-80C2A2	2GE037
A318	CFM56-5B9	CFM56-5B9/3	8CM060
A319	IAE V2522-A5	V2522-A5 SelectOne™ Upgrade Package	10IA011
A321	CFM56 5B	CFM56-5B1/3	8CM052
A332	Trent 772B	Trent 772	14RR071
A333	CF6-80E1A2	CF6-80E1A2	1GE033
A342	CFM56-5C4	CFM56-5C4	2CM015
A343	CFM56-5C2	CFM56-5C2	1CM010
A345	Trent 553	Trent 553-61	8RR044
A346	Trent 556	Trent 556-61	8RR045
A3ST	CF6-80C2A8	CF6-80C2A8	2GE040
B722	JT8D-15	JT8D-15	1PW010
B733	CFM56-3B-2	CFM56-3B-2	1CM005
B735	CFM56-3C-1	CFM56-3C-1	1CM007
B739	CFM56-7B27	CFM56-7B27	3CM034
B743	CF6-50E2	CF6-50E2	1GE009
B744	CF6-80C2B1F	CF6-80C2B1F	2GE045
B748	GENX-2B67	GEnx-2B67B	13GE157
B752	RB211-535E4	RB211-535E4	3RR028
B763	PW4060	PW4060	12PW101
B772	GE90-90B	GE90-90B	6GE090
B77L	GE90-110B1L	GE90-110B1	7GE097
B77W	GE90-115BL	GE90-115B	7GE099
B788	Trent 1000-A	Trent 1000-A	11RR049
B789	Trent 1000-AE	Trent 1000-AE3	19RR085
BA11	RR Spey 163.25	SPEY Mk555	1RR018
BE40	JT15D-5R	JT15D-5, -5A, -5B	1PW037

C550	JT15D-4	JT15D-4 series	1PW036
C551	JT15D-4	JT15D-4 series	1PW036
C560	JT15D-5A	JT15D-5, -5A, -5B	1PW037
C680	PW306C	PW306B	7PW078
C750	AE3007C	AE3007C2	13AL027
CRJ1	CF34-3A1	CF34-3A1	1GE035
CRJ2	CF34-3B1	CF34-3B	5GE084
CRJ9	CF34-8C5	CF34-8C5	8GE110
D228	GARRETT TPE 331-5-252D	TFE731-3	1AS002
DC10	CF6-50C2	CF6-50C2	3GE074
DC93	JT8D-11	JT8D-11	1PW008
DC94	JT8D-11	JT8D-11	1PW008
E135	AE2007A3	AE3007A3	6AL019
E145	AE3007A1	AE3007A1	6AL007
E170	CF34-8E5	CF34-8E5	8GE108
E190	CF34-10E6	CF34-10E6	10GE131
E35L	AE3007A1E	AE3007A1E	6AL020
E550	AS907-3-1E	HTF7500E (AS907-3-1E-A1)	14HN006
F100	TAY Mk620-15	TAY Mk620-15	1RR020
F28	RR	SPEY Mk555	1RR018
F2TH	PW308C	PW308C	7PW080
F70	TAY Mk620-15	TAY Mk620-15	1RR020
F900	TFE731-40	TFE731-3	1AS002
FA50	TFE731-40	TFE731-3	1AS002
FA7X	PW307A	PW307A	8PW091
GL5T	BR700-710A2-20	BR700-710A2-20	4BR009
GLEX	BR700-710A2-20	BR700-710A2-20	4BR009
GLF5	BR700-710C4-11	BR700-710C4-11	6BR010
HA4T	PW308A	PW308A	7PW079
IL76	D-30KP-II	D-30KP-2	1AA002
IL96	PS-90A	PS-90A	13AA006
L101	RB 211-22B	RB211-22B	1RR002
LJ35	GARETT TFE 731-22B	TFE731-2-2B	1AS001
MD11	PW4460	PW4460	1PW052

MD82	JT8D-217C	JT8D-217C	4PW070
MD83	JT8D-219	JT8D-219	4PW071
SU95	SaM146-1S17	SaM146-1S17	11PJ001
T134	Soloviev D30-III	D-30 (II series)	1AA001
T154	Soloviev D-30KU-154-II	D-30KU-154	1AA004
T204	PS-90A	PS-90A	13AA006

D. Summary of Boeing Fuel Flow Method 2

An outline of the Boeing Fuel Flow Method 2 (Dubois et al., 2006; Baughcum et al., 1996) as applied to extrapolating NO_x emissions from LTO to cruise conditions is included below. A more detailed analysis can be found in NASA's Scheduled Civil Aircraft Emission Inventories for 1992, Appendix D or Boeing's "Fuel Flow Method2" for Estimating Aircraft Emissions.

First, apply corrections for installation effects to the measured fuel flow reported in the EDB.

Table A-3: BFFM2 Installation Corrections

Power Setting	Correction
Take-off	1.010
Climb Out	1.013
Approach	1.020
Idle	1.100

On a log-log scale, apply a linear fit through the NO_x Emissions Indices reported in the EDB vs the corrected fuel flows from above.

Calculate a Fuel Flow Factor, W_{ff}, using delta and theta corrections for temperature and pressure at altitude, and known cruise fuel flow using

$$W_{ff} = \frac{W_f}{\delta_{\mathrm{amb}}} \theta_{\mathrm{amb}}^{3.8} e^{0.2M^2}$$

where theta is defined as

$$\Theta_{\mathrm{amb}} = \frac{T_{\mathrm{amb}} + 273.15}{288.15}$$

and delta is defined as

$$\delta_{\text{amb}} = \frac{P_{\text{amb}}}{14.696}$$

Next, calculate the new cruise NO_x emissions index, $(\text{EINO}_\text{x})_{W_{ff}}$, from W_{ff} and the log-log linear fit, then apply the following relationships and corrections

$$\text{EINO}_\text{x} = (\text{EINO}_\text{x})_{W_{ff}}\, e^{H} \left(\frac{\delta_{\text{amb}}^{1.02}}{\Theta_{\text{amb}}^{3.3}}\right)^{0.5}$$

where

$$H = -19.0(\omega - 0.0063, \quad \omega = \frac{0.62198(\Phi)\text{P}_\text{v}}{P_{\text{amb}} - (\Phi)\text{P}_\text{v}}, \quad P_v = (0.14504)10^{\beta}$$

and

$$\beta = 7.90298\left(1 - \frac{373.16}{T_{\text{amb}} + 273.16}\right) + 3.00571 + (5.02808)\log\left(\frac{373.16}{T_{\text{amb}} + 273.16}\right)$$
$$+ (1.3816 * 10^{-7})\left[1 - 10^{11.344\left(1 - \frac{T_{\text{amb}} + 273.16}{373.16}\right)}\right]$$
$$+ (8.1328 * 10^{-3})\left[10^{3.49149\left(1 - \frac{373.16}{T_{\text{amb}} + 273.16}\right)} - 1\right]$$

A visual representation of this method is included below for reference, where the blue circles are the original EDB values, the pink shows the fuel flow factor look-up on the log-log fit, and the green shows the final Emissions Index.

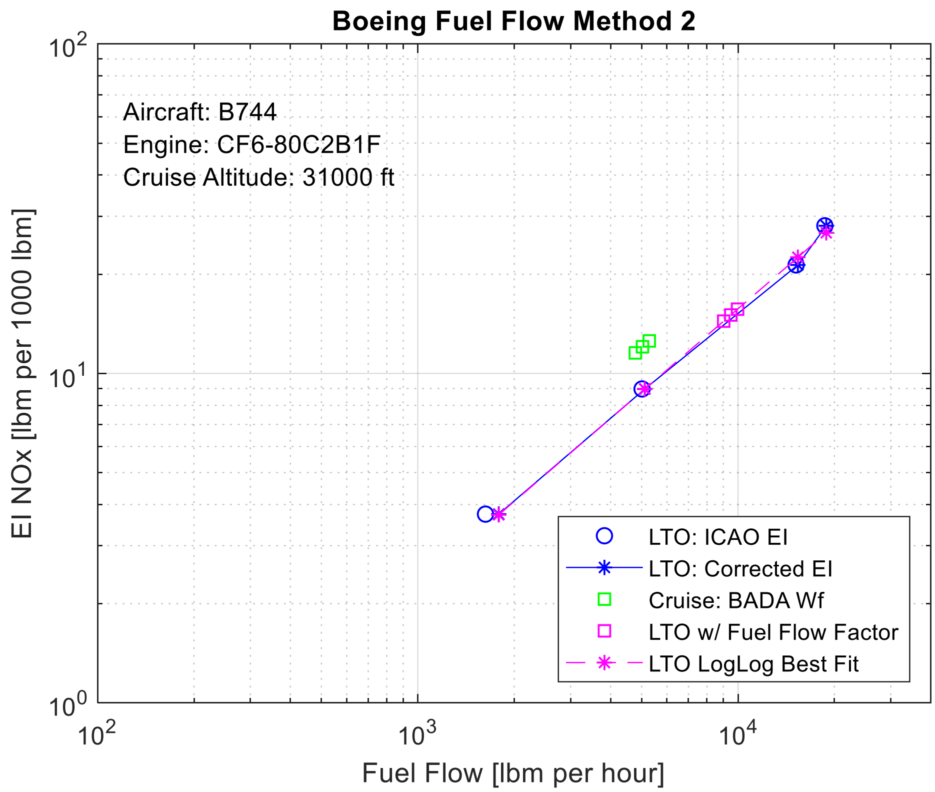

Figure A-13: Example of BFFM2 Compared to EDB Data for B744 Aircraft

E. Cycle Efficiency Equations

Cycle equations used to represent cycle efficiency, and thrust as outlined in Cumpsty and Heyes (2015) are included here. First, net power is defined as the difference in work done in the turbine and work done in the compressor, which assumes net power is used for propulsion.

$$\dot{W}_{\text{net}} = \dot{W}_{\text{turb}} - \dot{W}_{\text{comp}}$$

Ideal work across the compressor is defined as

$$\dot{W}_{\text{comp}} = \dot{m}_{\text{air}} C_p \,(T_3 - T_2)$$

where $\dot{m}_{\text{air}}$ is the mass flow rate, c_p is the specific heat of air, and the temperature change across the compressor is represented by T_3 and T_2. Isentropic temperature change can be represented with pressure ratio for an adiabatic process, and real work is represented by

$$\dot{W}_{\text{comp}} = \frac{\dot{m}_{\text{air}} C_p T_2 \,\left(\text{PR}^{\left(\gamma - \frac{1}{\gamma}\right)} - 1\right)}{\eta_{\text{comp}}}$$

which incorporates a compressor efficiency.

The ideal work across the turbine is defined as

$$\dot{W}_{\text{turb}} = \dot{m}_{\text{air}} C_p (T_4 - T_5)$$

with all the same definitions as above. Again, isentropic temperature change can be represented with pressure ratio for an adiabatic process, and real work is represented by

$$\dot{W}_{\text{turb}} = \eta_{\text{turb}} \dot{m}_{\text{air}} C_p T_4 \left(1 - \text{PR}^{-\left(\gamma - \frac{1}{\gamma}\right)}\right)$$

which incorporates turbine efficiency.

Going back to the original definition for net work, and combining the two previous expressions for real work, yields

$$\frac{\dot{W}_{\text{net}}}{\dot{m}_{\text{air}} C_p T_2} = \left(\eta_{\text{turb}} \frac{T_4}{T_2} \left(1 - \frac{1}{\text{PR}^{\left(\gamma - \frac{1}{\gamma}\right)}} \right) - \frac{\text{PR}^{\left(\gamma - \frac{1}{\gamma}\right)} - 1}{\eta_{\text{comp}}} \right)$$

where specific work is only a function of four assumptions.

Finally, the cycle efficiency can be defined as

$$\eta_{\text{cycle}} = \frac{\dot{W}_{\text{net}}}{\dot{m}_{\text{air}} C_p (T_4 - T_3)}$$

where the numerator represents the net power out and the denominator represents power from the combustor.

Replacing the T_3 terms with

$$(T_4 - T_3) = T_2 \left(\frac{T_4}{T_2} - \frac{T_3}{T_2} \right)$$

and

$$\frac{T_3}{T_2} = 1 + \frac{\text{PR}^{\gamma - 1/\gamma} - 1}{\eta_{\text{comp}}}$$

eliminates one unknown in the expression for cycle efficiency. The others are eliminated by substituting the specific work term already derived, and cycle efficiency can be represented as

$$\eta_{\text{cycle}} = \left(\eta_{\text{turb}} \frac{T_4}{T_2} \left(1 - \frac{1}{\text{PR}^{\left(\gamma - \frac{1}{\gamma}\right)}} \right) - \frac{\text{PR}^{\left(\gamma - \frac{1}{\gamma}\right)} - 1}{\eta_{\text{comp}}} \right) * \frac{1}{\left(\frac{T_4}{T_2} - \left(1 + \frac{PR^{\gamma - \frac{1}{\gamma}} - 1}{\eta_{\text{comp}}} \right) \right)}$$

based on the same four assumptions of temperature ratio, compressor efficiency, turbine efficiency and propulsive efficiency.

Thrust is calculated as

$$\text{Thrust} = \frac{\eta_{\text{overall}} * W_f * \text{LHV}}{\text{Velocity}}$$

using an overall efficiency, which includes both cycle and propulsive, a fuel flow rate, the lower heating value of the fuel, and the velocity.

Next, the CO_2 emission rate at cruise per unit thrust is defined as

$$\text{CO}_2 \text{ Emissions Rate per Unit Thrust} = \frac{\text{EI}_{\text{CO}_2}}{\left(\eta_{\text{cycle}} * \eta_{\text{prop}}\right) * \text{LHV} * \frac{1}{\text{Velocity}}}$$

using the terms for cycle efficiency and thrust from above.

Finally, a lapse rate between cruise thrust and rated thrust can be estimated as the change in air density. Although more complex assumptions can be made, such as including effects of by-pass ratio on lapse rate, this simple relationship can be used when little information is available.

Figure A-14 shows the results of this analysis using 10,000 Monte Carlo runs and a range of assumptions listed in Table 1. For comparison, two representative engine models from a major gas turbine manufacture have been included. The red data represents 1990’s technology, while the blue data represents a 2010’s engine.

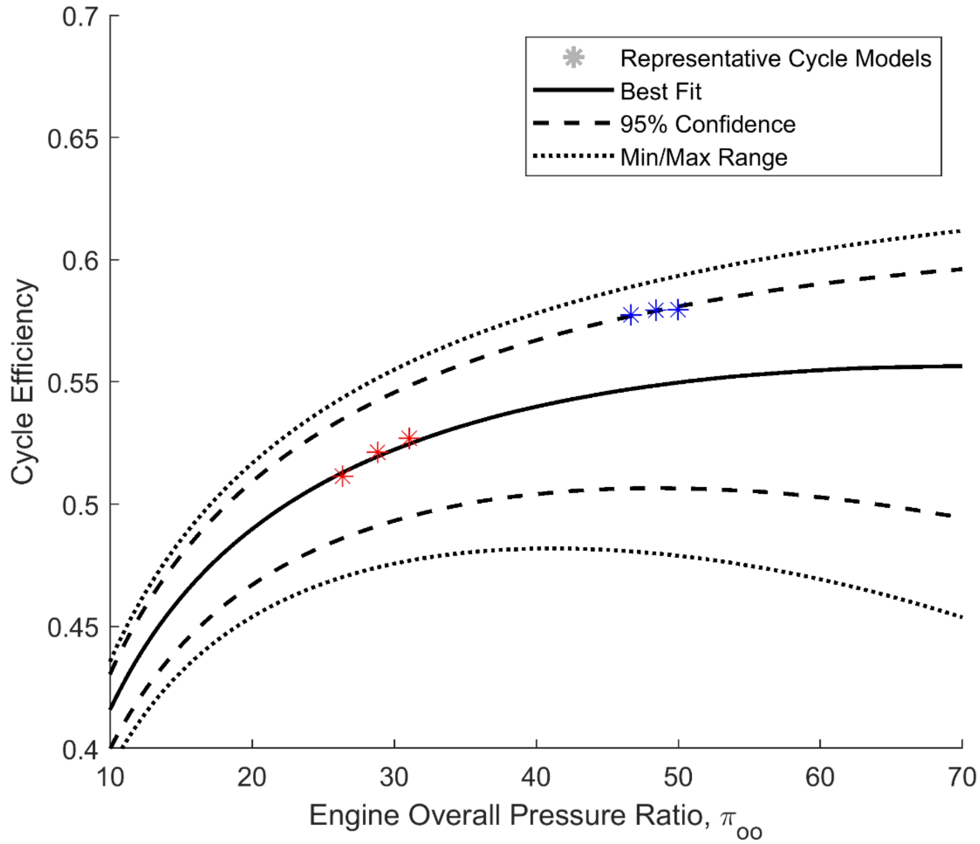

Figure A-14: Cycle efficiency vs OPR with representative cycle model output for comparison

F. Climate and Air Quality Damages

Table A-4: Cruise Results with Uncertainty (Grobler et al. 2019)

		Climate					Air Quality	
		2% Disc. Rate	**2.5% D.R.**	**3% D.R.**	**5% D.R**	**7% D.R.**	**Variable VSL**	**Constant VSL**
CO_2	[$/tonne CO_2]	95 (14, 250)	62 (9.3, 160)	45 (6.7, 120)	17 (2.7, 44)	9.4 (1.5, 23)	N/A	N/A
NO_x: CH_4	[$/tonne NO_x as NO_2]	-2900 (-7800, -420)	-2500 (-6600, -370)	-2200 (-5700, -330)	-1500 (-3700, -230)	-1100 (-2600, -170)	N/A	N/A
NO_x: O_3 Short	[$/tonne NO_x as NO_2]	3300 (430, 9200)	2900 (390, 8000)	2700 (370, 7200)	2200 (320, 5600)	1900 (290, 4800)	N/A	N/A
NO_x: O_3 Long	[$/tonne NO_x as NO_2]	-950 (-2600, -120)	-810 (-2200, -110)	-720 (-1900, -96)	-480 (-1300, -67)	-350 (-900, -50)	N/A	N/A
NO_x: Nitrate Aerosols	[$/tonne NO_x as NO_2]	-860 (-2400, -110)	-760 (-2100, -100)	-700 (-1900, -94)	-570 (-1500, -81)	-500 (-1300, -73)	N/A	N/A
NO_x: Total	[$/tonne NO_x as NO_2]	-1400 (-3900, -200)	-1200 (-3100, -160)	-940 (-2600, -120)	-340 (-1200, 54)	-20 (-590, 460)	21000 (3600, 66000)	21000 (3700, 67000)

Table A-5: Landing and Take-off Results with Uncertainty (Grobler et al. 2019)

CO_2	[$/tonne CO_2]	95 (14, 250)	63 (9.2, 160)	45 (6.7, 120)	17 (2.7, 44)	9.5 (1.5, 23)	N/A	N/A
NO_x: CH_4	[$/tonne NO_x as NO_2]	-550 (-1500, -78)	-470 (-1200, -68)	-410 (-1100, -61)	-270 (-690, -42)	-200 (-490, -32)	N/A	N/A
NO_x: O_3 Short	[$/tonne NO_x as NO_2]	390 (54, 1100)	350 (49, 940)	320 (46, 850)	260 (40, 660)	230 (36, 560)	N/A	N/A
NO_x: O_3 Long	[$/tonne NO_x as NO_2]	-180 (-490, -26)	-160 (-410, -23)	-140 (-360, -20)	-91 (-230, -14)	-66 (-160, -11)	N/A	N/A
NO_x: Nitrate Aerosols	[$/tonne NO_x as NO_2]	-440 (-1300, -47)	-400 (-1100, -43)	-360 (-1000, -41)	-300 (-810, -35)	-260 (-690, -32)	N/A	N/A
NO_x: Total	[$/tonne NO_x as NO_2]	-780 (-2200, -100)	-670 (-1800, -91)	-590 (-1600, -81)	-400 (-1100, -55)	-290 (-780, -40)	37000 (5900, 98000)	26000 (4600, 83000)

G. Lerner Index and Markups

The Lerner Index is a measure of market power, between 0 and 1, where higher values represent greater market power. It is a function of the market price of an item, and the marginal cost of production. This relationship can be rearranged to solve for the markup of a product, defined as the marginal cost over the market price.

$$L = \frac{P - MC}{P} \rightarrow \frac{MC}{P} = (1 - L)$$

Using 4.75 (Khan et al., 2013) and 1.76 (Considine, 2001) as bounds, a range of marginal costs are drawn compared to the market price of Jet A from ThomsonOne.

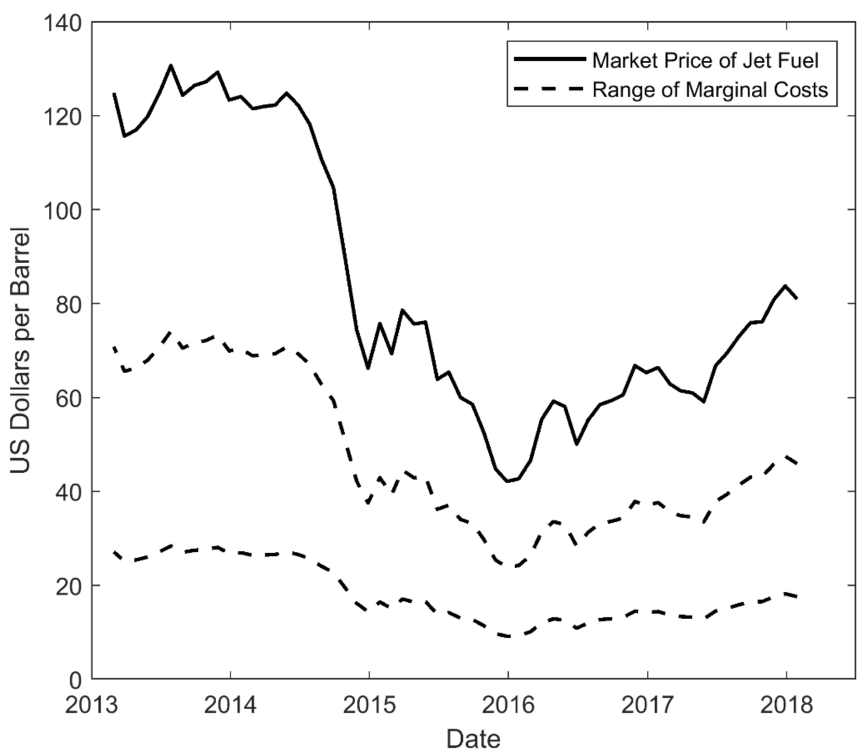

Figure A-15: The market price and marginal cost of jet fuel between 2013 and 2018

Figure A-16 and Figure A-17 show the distribution of costs per the data above, and the Monte Carlo draws used to represent that data.

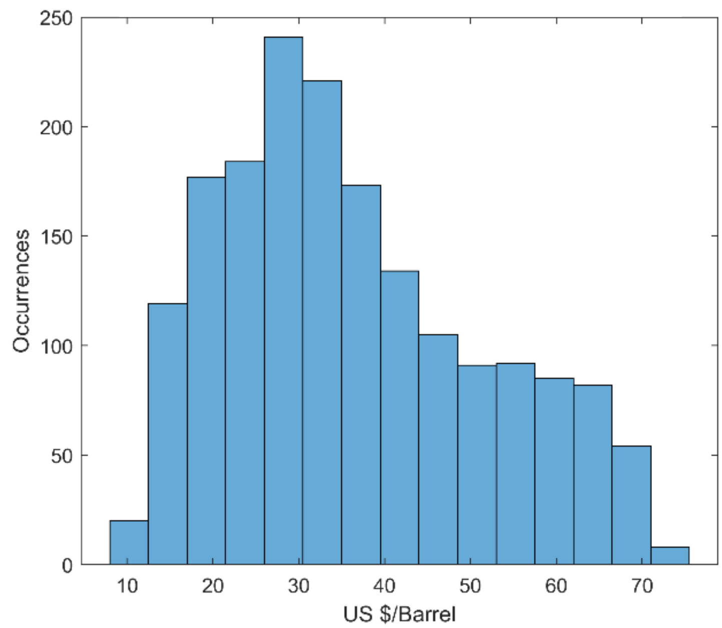

Figure A-16: Distribution of marginal cost of jet fuel production from 2013-2018

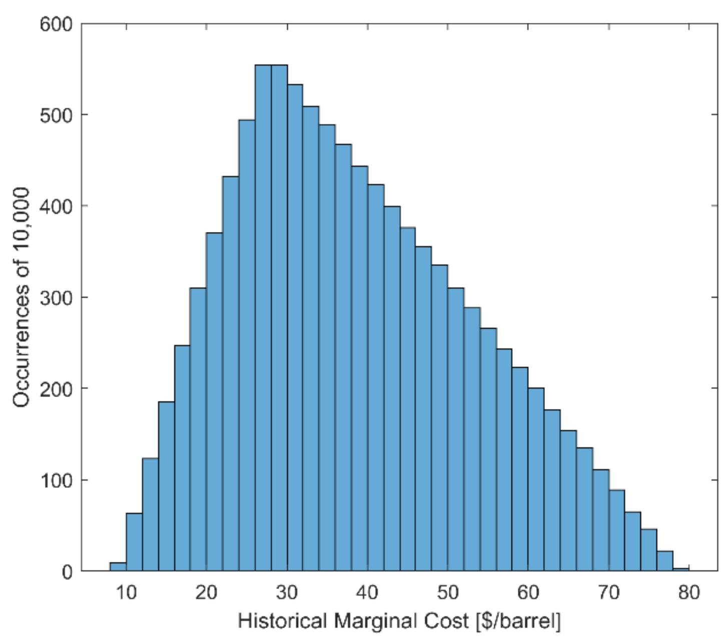

Figure A-17: Monte Carlo draws used to represent the marginal cost of jet fuel from 2013-2018

H. Time in Cruise for 2013 Flights

AEIC is used to find a distribution of time in cruise for all flights in 2013, the last reference year available in AEIC V3.0. The time in cruise is then combined with a constant assumed time in LTO of 2,897s (0.8 hr) to get the time-split between LTO and cruise used in this analysis.

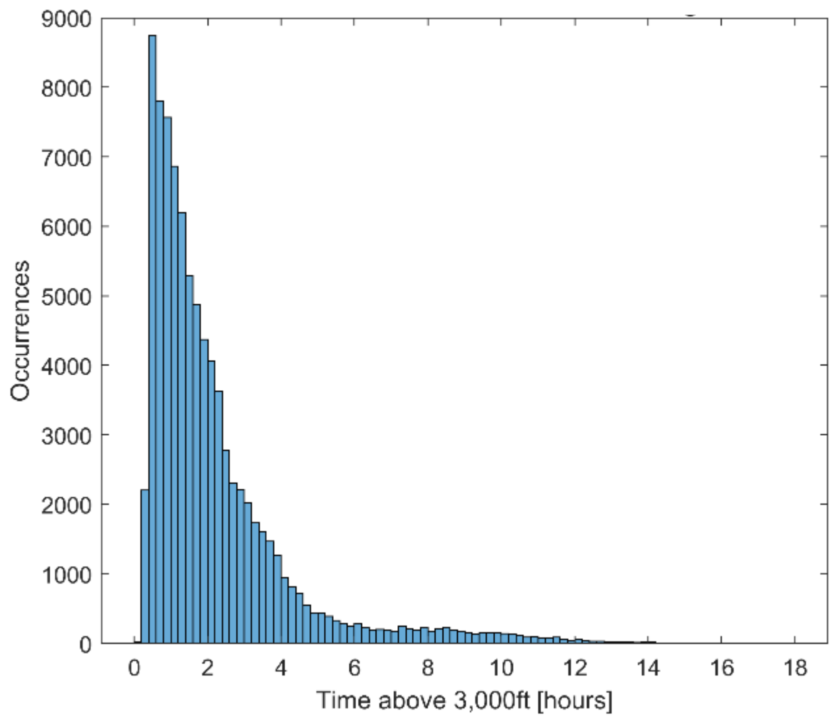

Figure A-18: Distribution of time in non-LTO operation for 2013 flights per AEIC

A triangular fit was used in the Monte Carlo draws to represent this data, shown in Figure A-19.

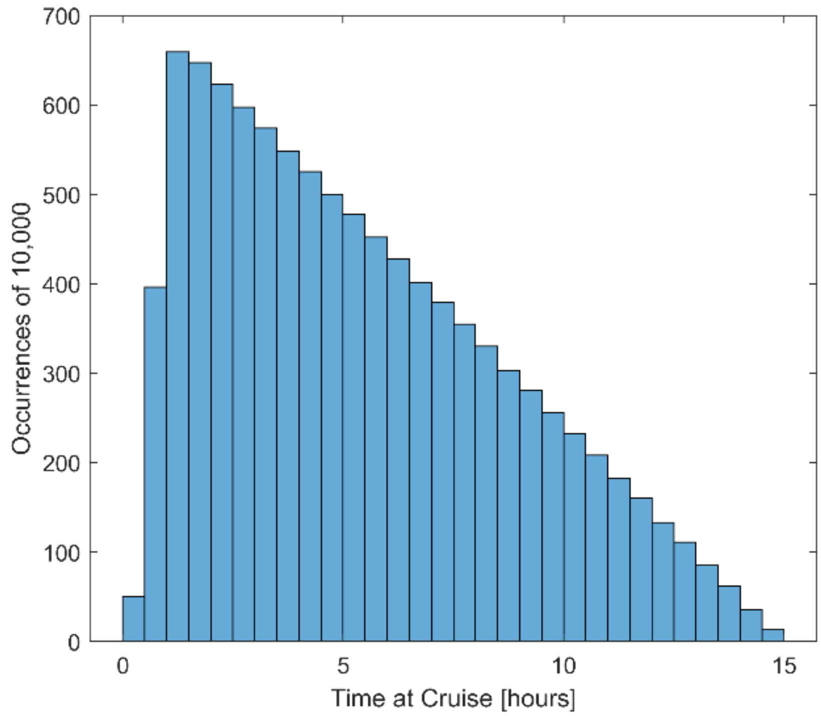

Figure A-19: Monte Carlo draws used to represent the time spent in cruise operation

I. <u>Distributions of Monte Carlo Inputs</u>

This section reviews Monte Carlo draws for non-uniform assumptions listed throughout the analysis. Figure A-20 includes three parts: the original figure for average cruise NO_x emissions (also Figure 3), the distribution of residuals from the data to the best fit line (lower left), and the Monte Carlo draws used for the 10,000 simulations (lower right).

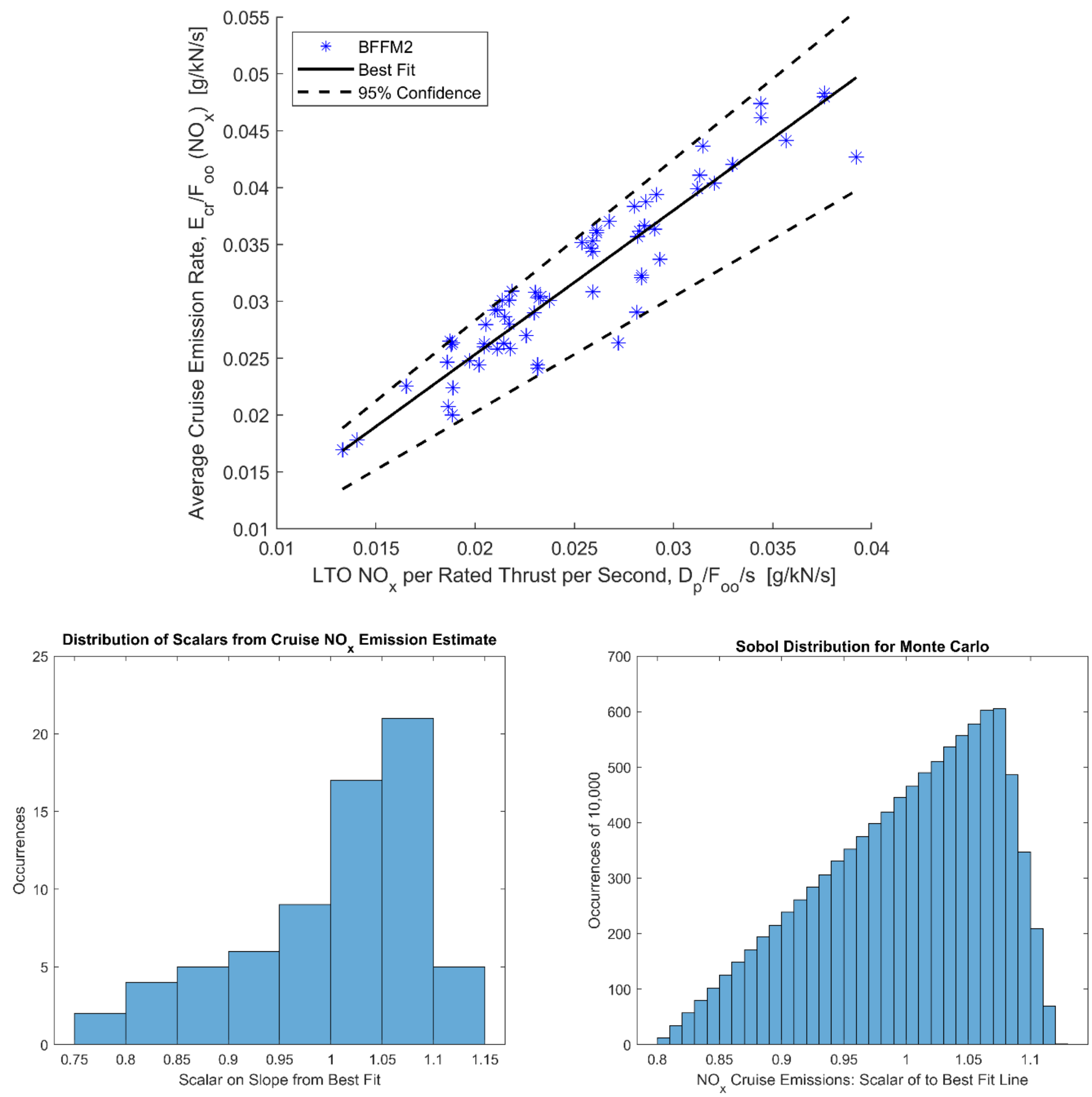

Figure A-20: Comparison of actual distribution to Monte Carlo draws for NO_x Cruise Emissions

Figure A-21 includes three parts: the original figure for average LTO CO_2 emissions (also Figure 2), the distribution of residuals from the data to the best fit line (lower left), and the Monte Carlo draws used for the 10,000 simulations (lower right).

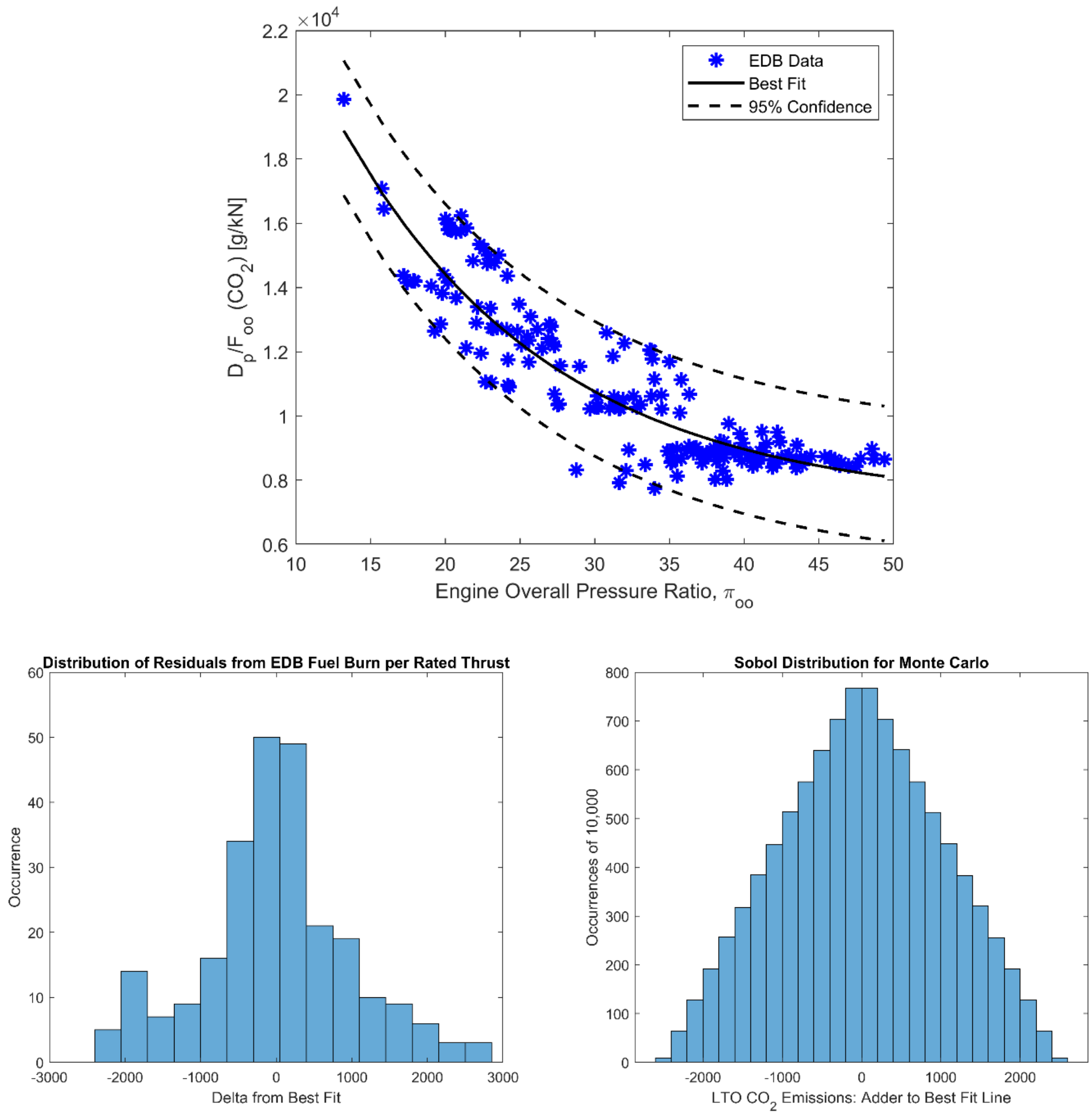

Figure A-21: Comparison of actual distribution to Monte Carlo draws for CO_2 LTO Emissions

J. Distribution of Damage Functions

The draws used in the Monte Carlo analysis for environmental damages are from a 100,000 sample run per Grobler et al. (2019). The distributions are included in Figures A-22 through A-27, from which the 10,000 draws were picked.

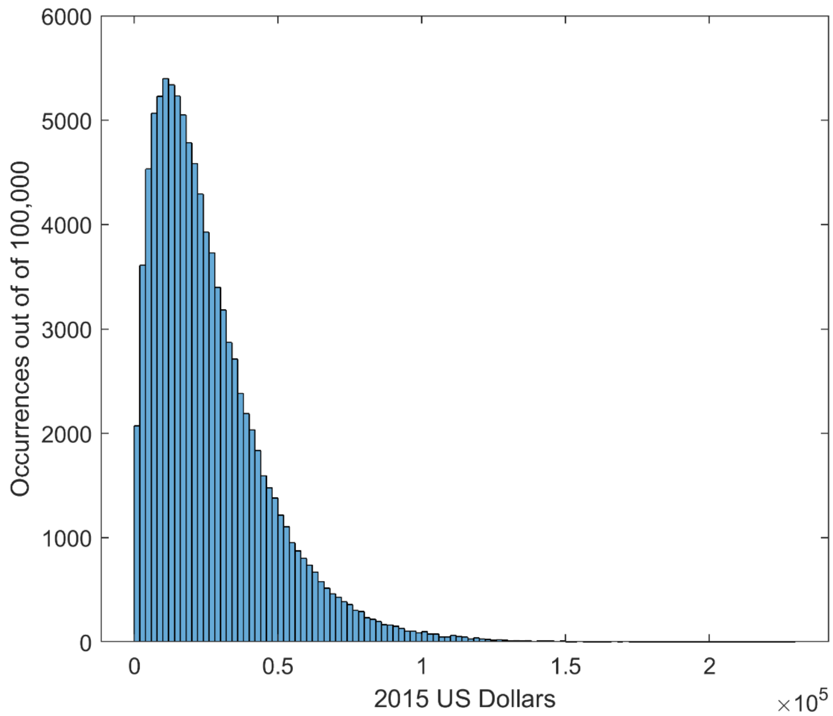

Figure A-22: Distribution of Air Quality Damage from NO_x Emissions at Cruise

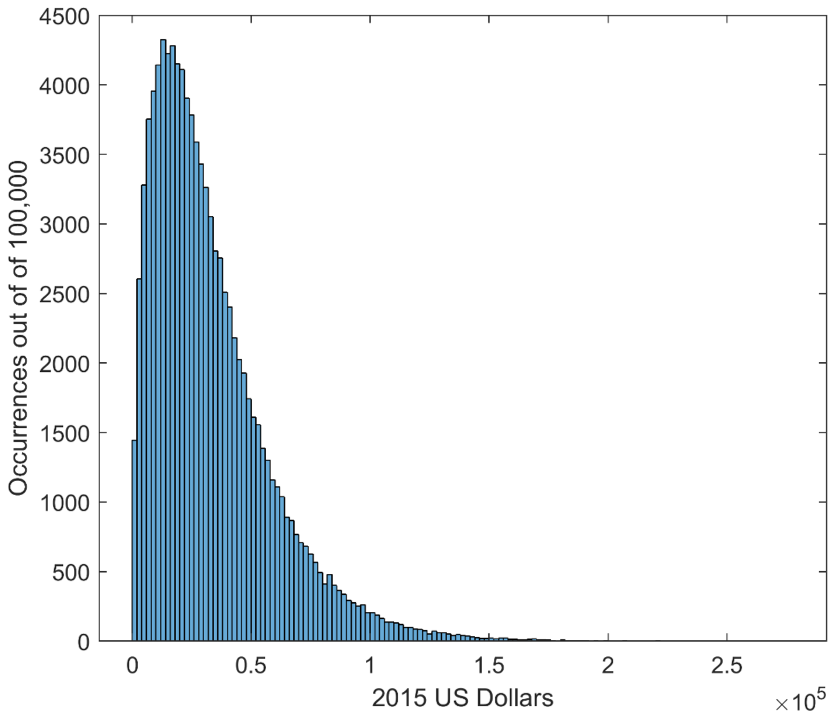

Figure A-23: Distribution of Air Quality Damage from NO_x Emissions in LTO

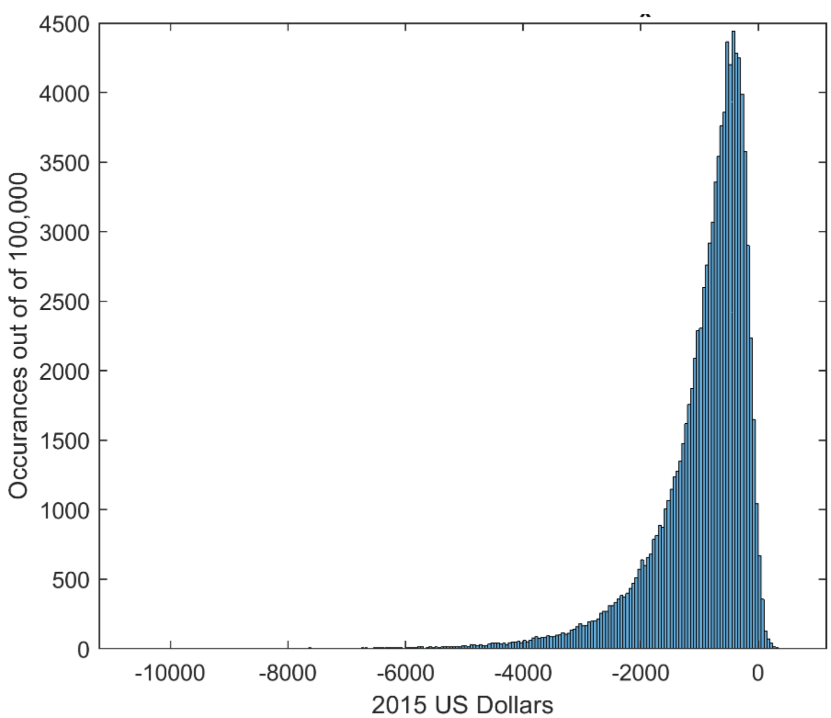

Figure A-24: Distribution of Climate Damage from NO_x Emissions in Cruise

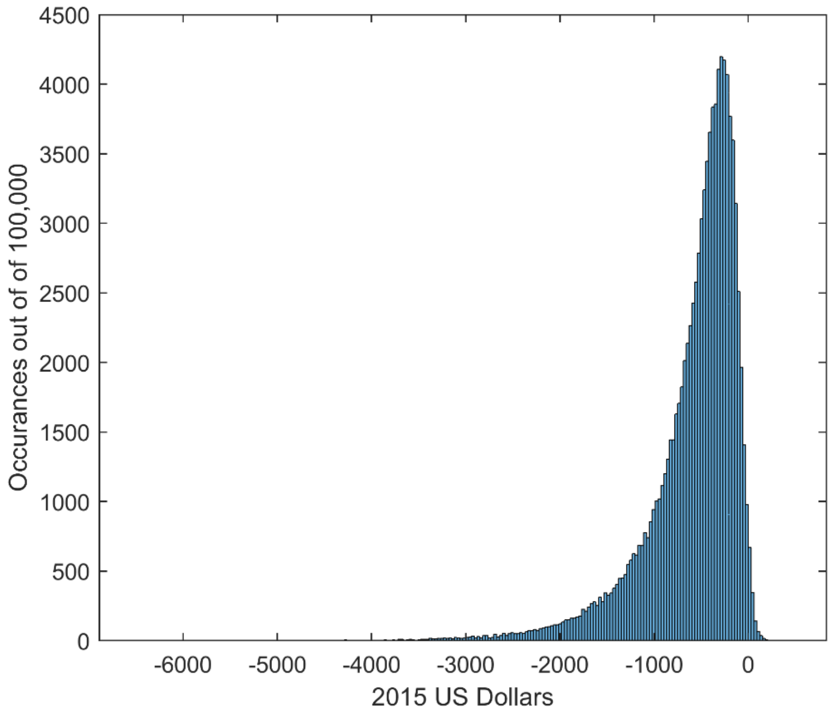

Figure A-25: Distribution of Climate Damage from NO_x Emissions in LTO Operation

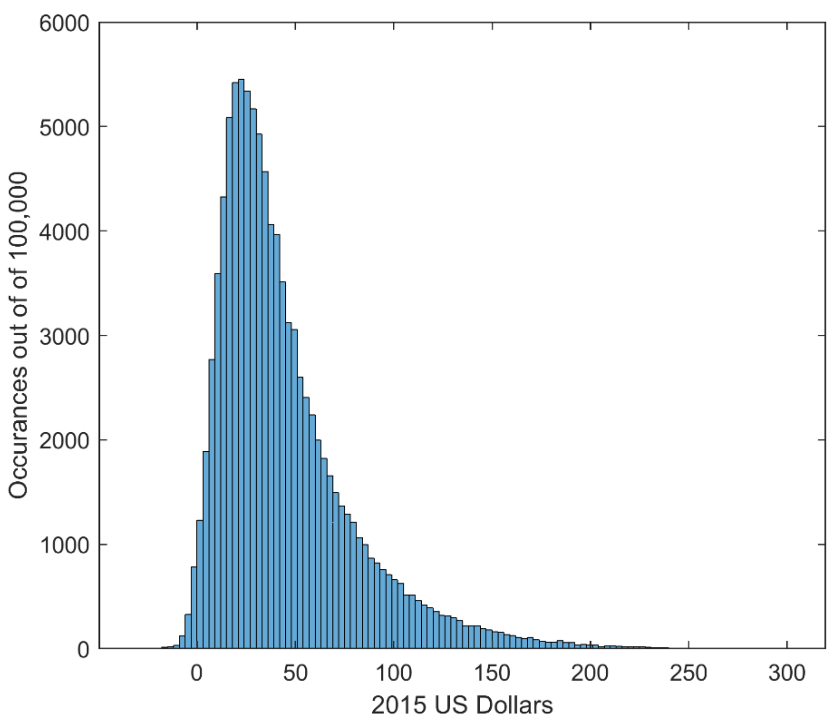

Figure A-26: Distribution of Climate Damage from CO_2 Emissions in Cruise

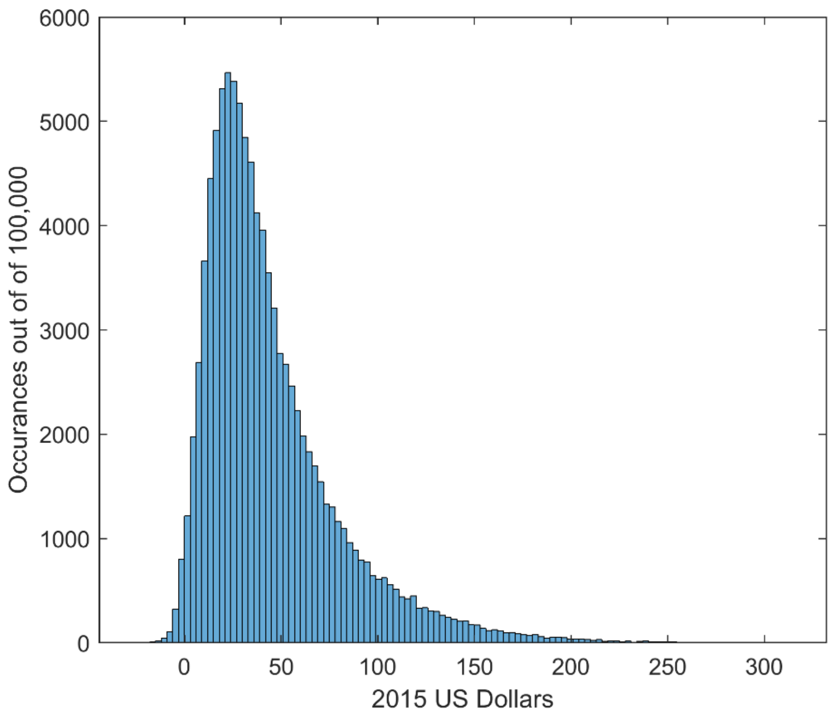

Figure A-27: Distribution of Climate Damage from CO_2 Emissions in LTO Operation

K. Fuel Costs, Climate Damage and Air Quality Damage for DR = 3.0%

For the results presented for the Monte Carlo analysis, and additional breakdown of LTO and cruise contributions are included below in Figures A-28 through A-30 for reference. The cruise contributions are higher than LTO because average cruise fuel flow rates are higher.

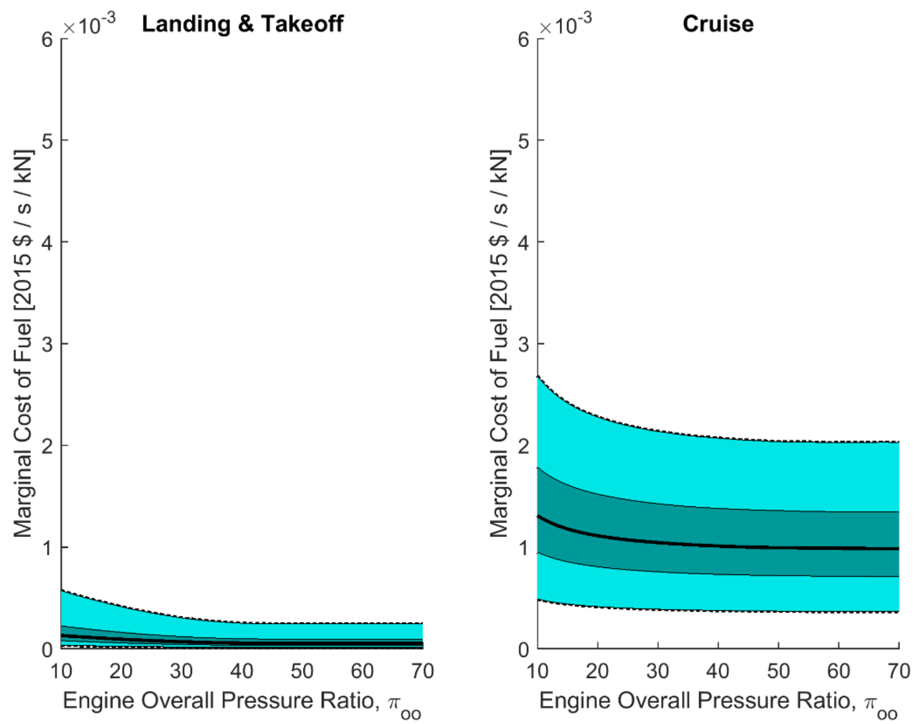

Figure A-28: Marginal Cost of Fuel per second of LTO and Cruise Operation

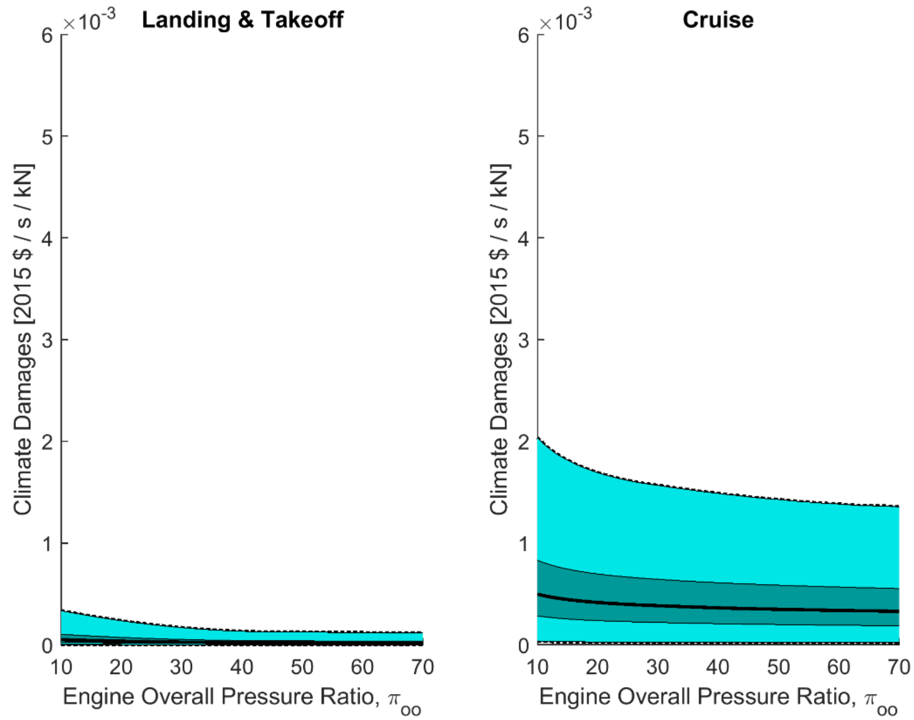

Figure A-29: Climate Damage per second of LTO and Cruise Operation

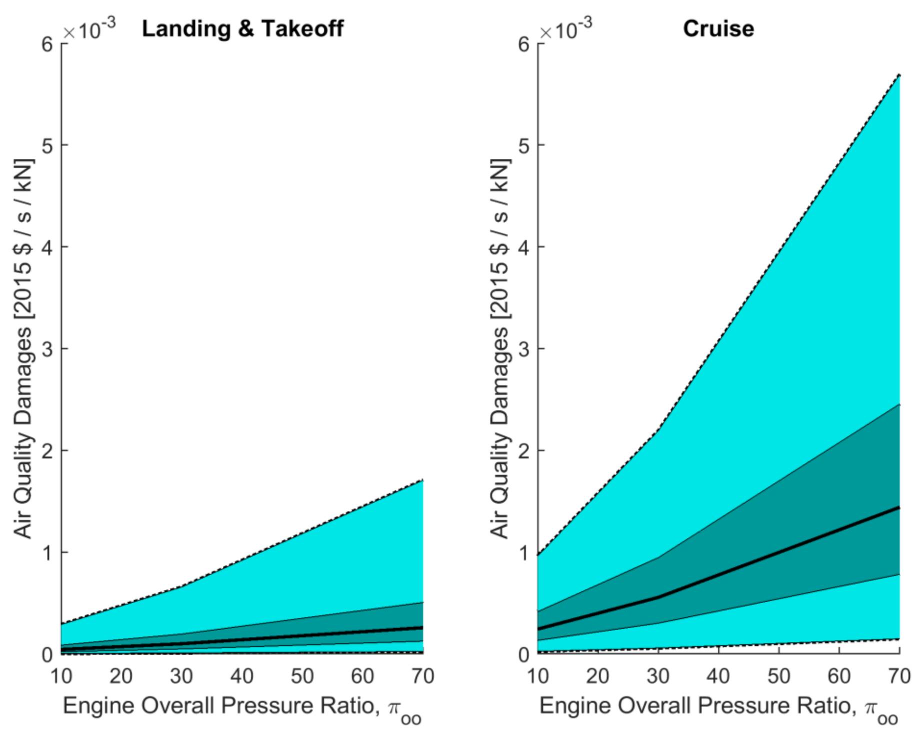

Figure A-30: Air Quality Damage per second of LTO and Cruise Operation

L. Sensitivity Analysis for Discount Rate = 3.0%

First-order and total-effect sensitivity are computed to determine the impacts of each unknown parameter, using the approach outlined below. Results show 80% of the uncertainty is associated with the monetized damage values from with emission levels, followed by 15% from the market price of jet fuel. This shows the analysis is stable with respect to emission level estimates, but widely impacted by the cost functions associated with those emissions. The equations for first-order and total-effect sensitivity are

$$S_i = \frac{\left(\frac{1}{\mathrm{N}}\right)\sum_{j=1}^{N} y_A^{(j)} y_{C_i}^{(j)} - f_0^2}{\left(\frac{1}{\mathrm{N}}\right)\sum_{j=1}^{N}\left(y_A^{(j)}\right)^2 - f_0^2}$$

and

$$S_{T_i} = 1 - \frac{\left(\frac{1}{\mathrm{N}}\right)\sum_{j=1}^{N} y_B^{(j)} y_{C_i}^{(j)} - f_0^2}{\left(\frac{1}{\mathrm{N}}\right)\sum_{j=1}^{N}\left(y_A^{(j)}\right)^2 - f_0^2}$$

respectively, where y_A, y_B and y_C are matrices of results, in this case social costs associated with different Monte Carlo runs. y_A and y_B are results from independent Sobol draws, and y_C are the results from replacing once variable at a time from y_A into y_B.

Table A-6: Sensitivity Analysis Results

Perturbation Parameter	First-Order Sensitivity @ OPR = 40	Total-Effect Sensitivity @ OPR = 40
Temperature Ratio	<1.0	<1.0%
Compressor Efficiency	<1.0	<1.0%
Turbine Efficiency	<1.0	<1.0%
Propulsive Efficiency	<1.0	<1.0%
NO_x Emissions in Cruise	<1.0	<1.0%
CO_2 Emissions in LTO	<1.0	<1.0%
Marginal Price of Jet Fuel	15.8%	15.9%
Time in Cruise	1.2%	2.1%
Environmental Damages	80.1%	81.6%

Results are also shown in the figures below, across all OPR ranges. It is easy to see here that almost all (>95%) of uncertainty is from monetizing damages, and less is from the emission calculations. As seen in the results, the production cost of fuel (in blue) is a high contributor at lower OPR, but air quality (combined here with climate) dominates at high OPR.

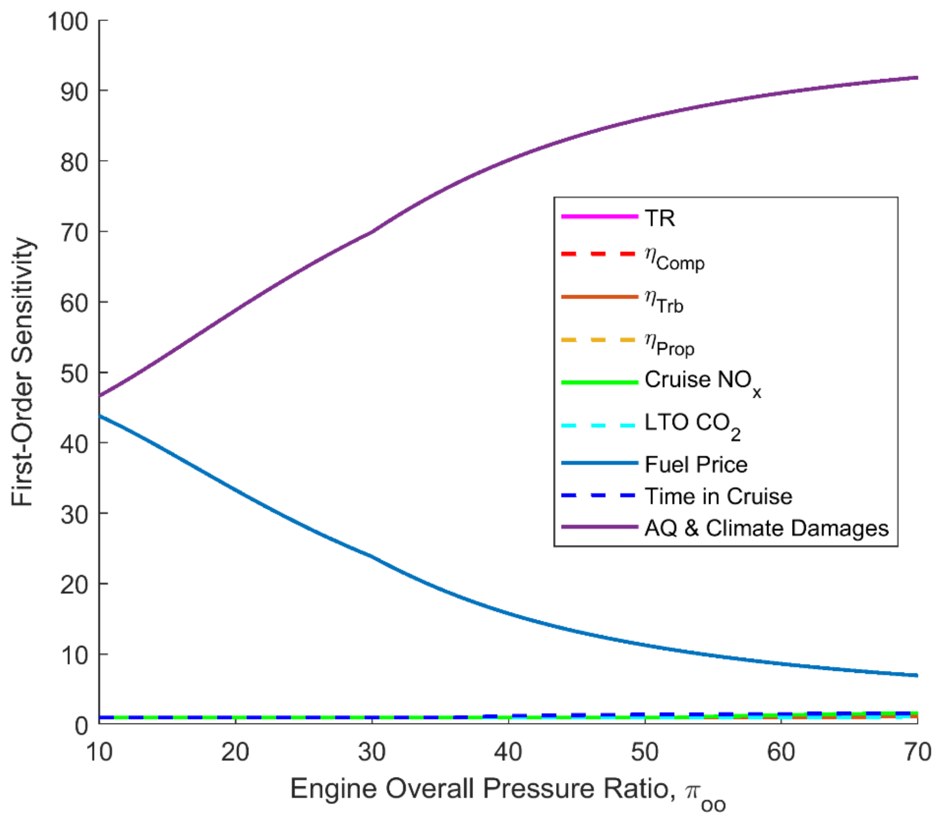

Figure A-31: First-orders sensitivity analysis for quantifying contributors to uncertainty

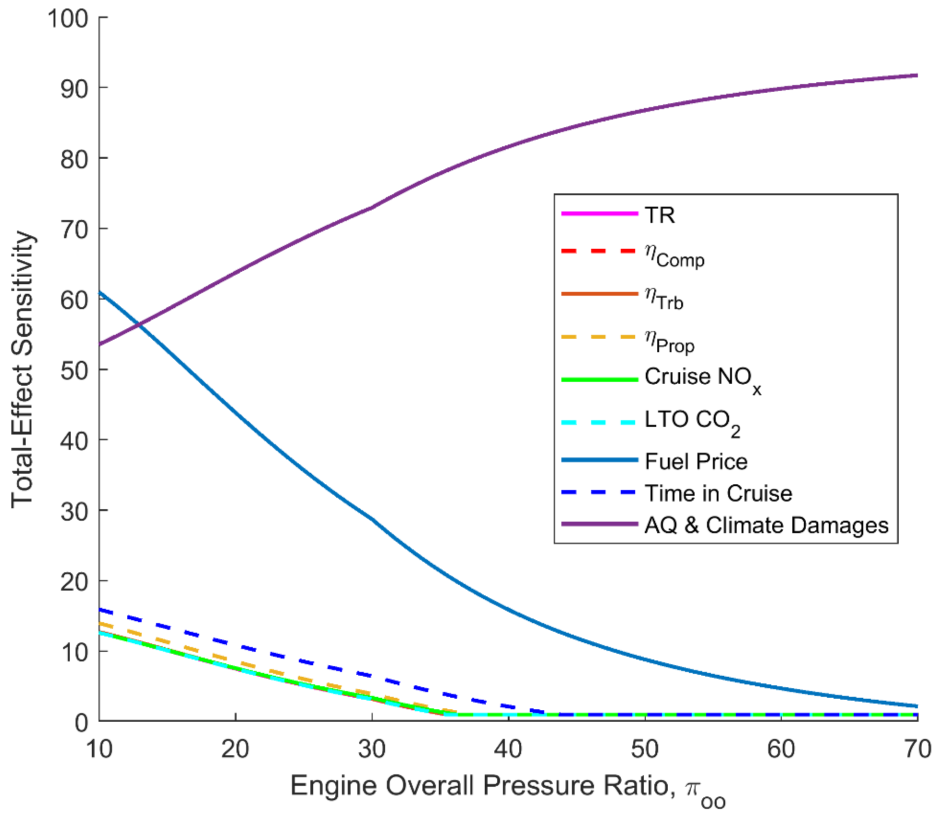

Figure A-32: Total-effect sensitivity analysis for quantifying contributors to uncertainty

M. Social Costs for Discount Rate = 2.0%

Finally, the same results discussed in the main body of text are shown again here, with a discount rate of 2.0% instead of 3.0%. All charts keep the same scale as the original results, showing a 2.0% discount rate yields overall higher social costs than 3.0%.

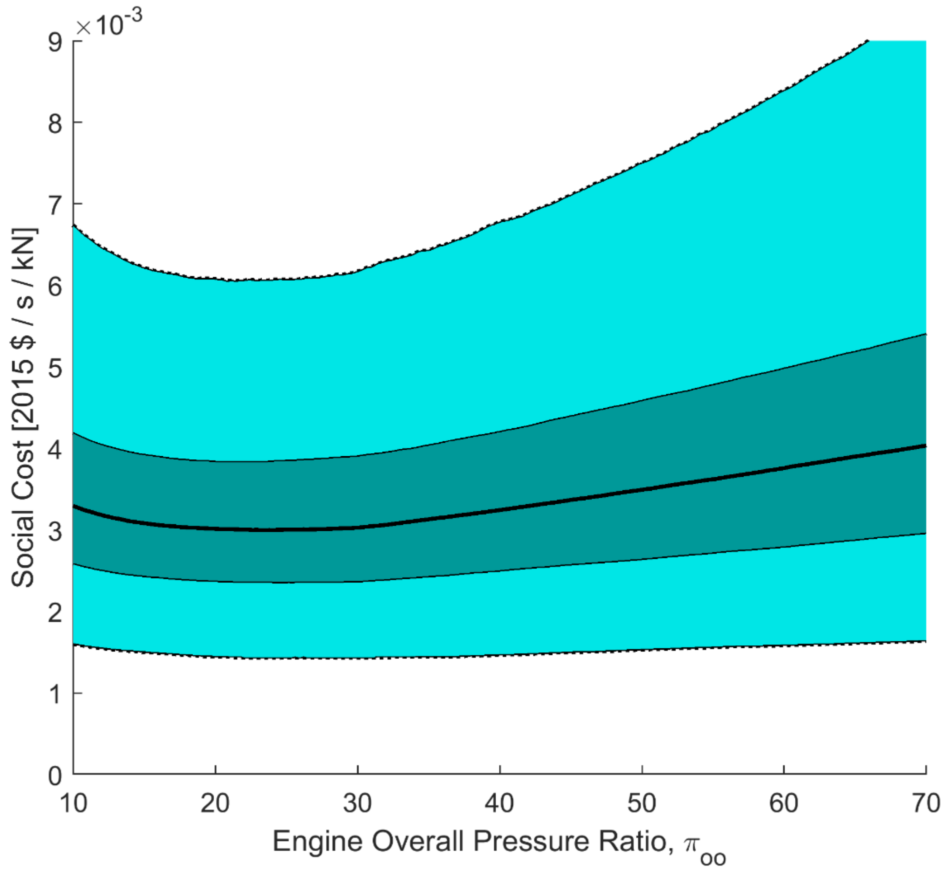

Figure A-33: Combined social cost analysis for a discount rate of 2.0%

Also included is the range of OPR corresponding to a minimum social cost in the 10,000 Monte Carlo runs. Here, 50% of results show social costs increasing by an OPR of 25 (as compared to 23) and 90% increasing by 42 (as compared to 36).

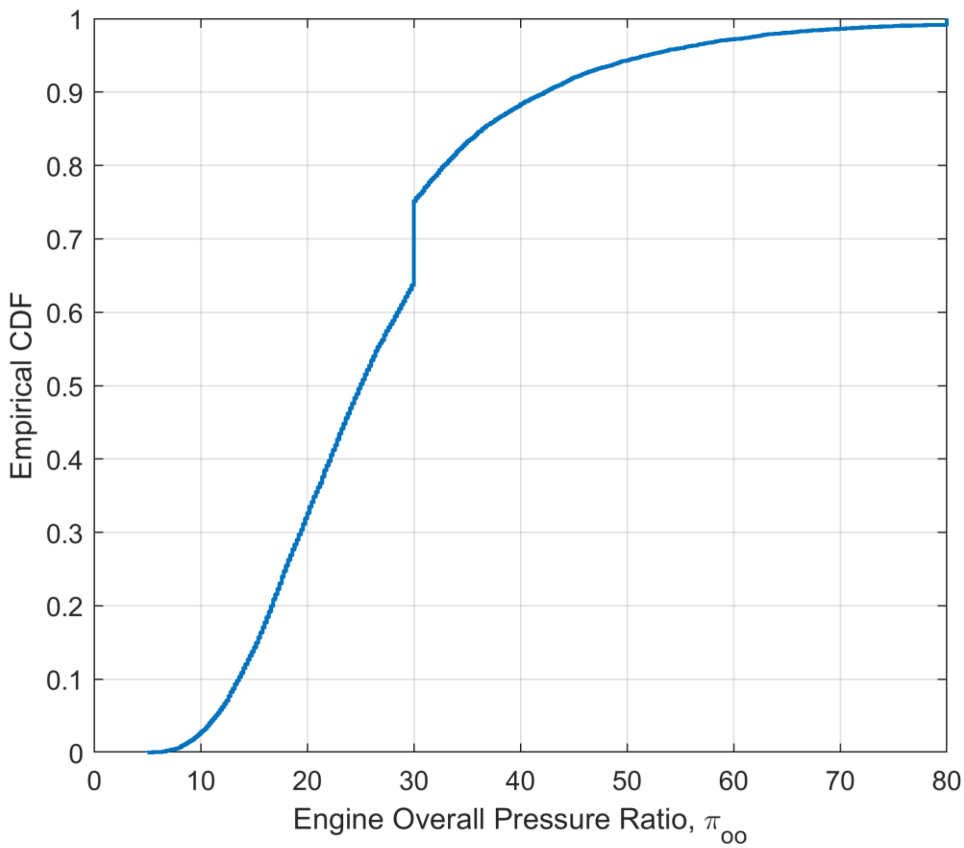

Figure A-34: Distribution of OPR for minimum social cost for a discount rate of 2.0%

N. Social Costs for Discount Rate = 7.0%

The same results discussed in the main body of text are shown again here, with a discount rate of 7.0% instead of 3.0%. All charts keep the same scale as the original results, showing a 7.0% discount rate yields overall lower social costs than 3.0%.

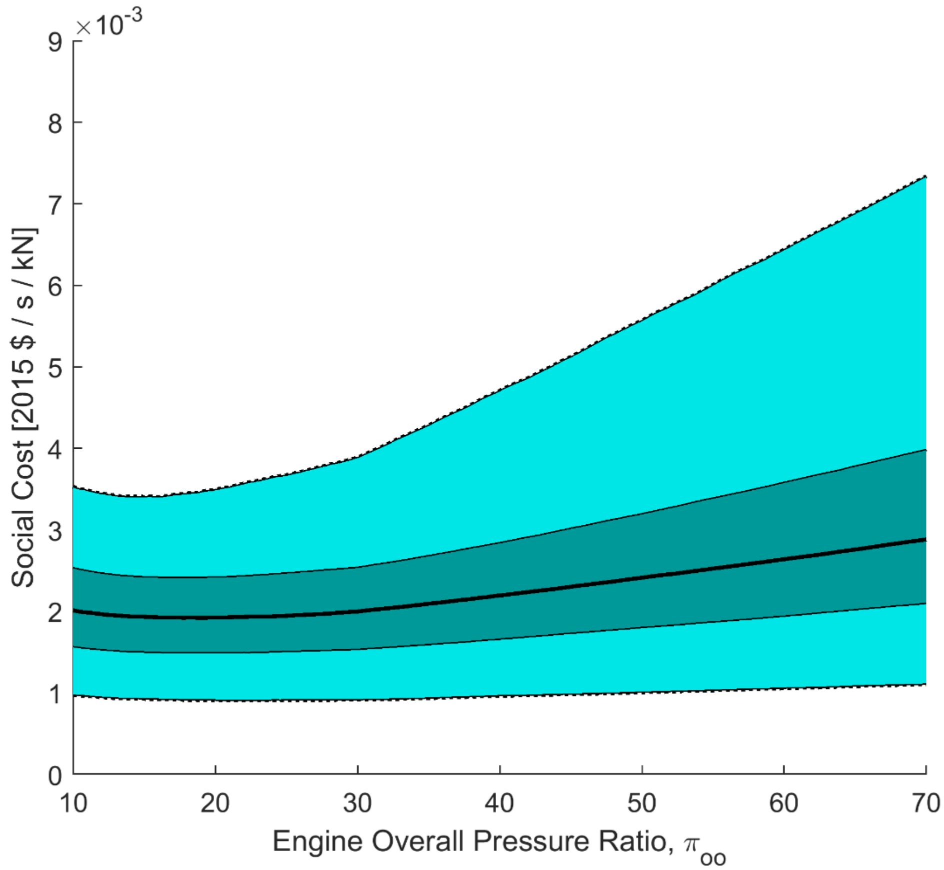

Figure A-35: Combined social cost analysis for a discount rate of 7.0%

Also included is the range of OPR corresponding to a minimum social cost in the 10,000 Monte Carlo runs. Here, 50% of results show social costs increasing by an OPR of 21 (as compared to 23) and 90% increasing by 32 (as compared to 36).

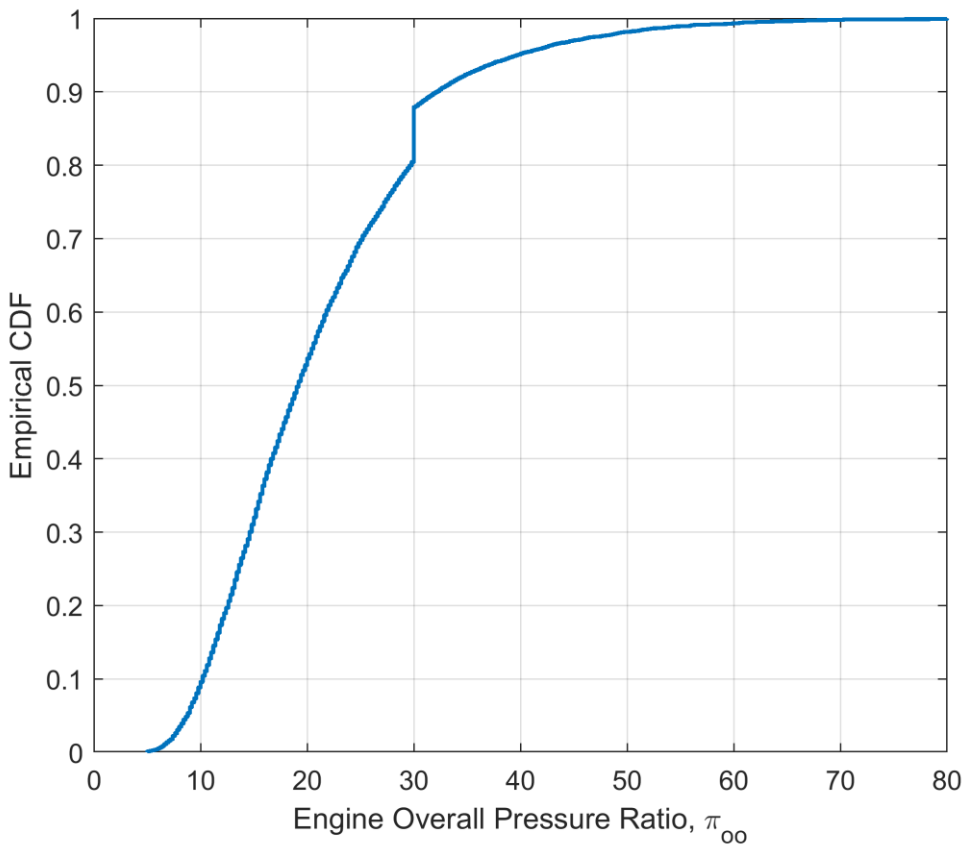

Figure A-36: Distribution of OPR for minimum social cost for a discount rate of 7.0%